JOURNAL OF GEOPHYSICAL RESEARCH, VOL. 113, C07015, doi:10.1029/2006JC003950, 2008

Infrared measurements of surface renewal and subsurface vortices in nearshore breaking waves

Yasunori Watanabe[1] and Nobuhito Mori[2]

Received 4 October 2006; revised 7 April 2008; accepted 30 April 2008; published 12 July 2008.

[1] When ocean waves reach a surf zone, jets projecting from the breakers splash sequentially, producing horizontal roller vortices beneath the jets and longitudinal counterrotating vortices behind the rollers; these vortices organize into three-dimensional structures that evolve into a turbulent bore with wave propagation. This disrupts any uniform temperature distributions on the surface, creating heterogeneous patterns of surface temperatures. In this study, we extracted surface temperature distributions from infrared measurements in small- and large-scale wave flumes, then used those data to study the renewed surfaces created by subsurface vortices beneath spilling and plunging breakers. In our large-scale experiments, temporal and spatial scales of surface renewal and surface recovery were consistent with earlier work; however, in our small-scale experiments, the spatial scales showed significant deviations from earlier in situ observations. These inconsistencies may be attributed to scale effects for subsurface vortices, and we show that the Froude number (Fr) can be used to characterize the initial formation of longitudinal counterrotating vortices. Further, for turbulent flows fully developed by wave breaking in a bore region, the frequency of surface renewal correlates exponentially with Reynolds number (Re). The computed vorticity on the breaking wave surface exhibits local patterns which correlate strongly with the gravity induced counterrotating vortices, which in turn renew the rear-facing surface of the breaking waves. In contrast the turbulent bore which precedes the wave crest rapidly disturbs and renews the surface in front of the crest. These two different mechanisms for surface renewal, during the nearshore breaking process, lead to modulations in the surface temperature distribution and changes in thermal diffusivity during the propagation of the breaking wave.

Citation: Watanabe, Y., and N. Mori (2008), Infrared measurements of surface renewal and subsurface vortices in nearshore breaking waves, *J. Geophys. Res.*, *113*, C07015, doi:10.1029/2006JC003950.

1. Introduction

[2] In a surf zone, waveshape and flow organization change substantially as breaking waves propagate. Free-surface dynamics in a surf zone, together with the resulting primary large-scale vortices, can be characterized by breaker type: typically either plunging or spilling breakers. In a plunging breaker, a wave crest begins to overturn at a breaking point, resulting in a transition from shoaling wave motion to rotational jetting flow in a breaking region. The overturning jet touches down on the forward water surface at a plunging point, forming a horizontal roller vortex that has its axis of rotation perpendicular to the wave direction; secondary jets successively produce an array of roller vortices. As dynamic splash-up continues in a plunging region (or in a transition region), successive plunging jets locally intensify strong turbulence, leading to fully developed turbulence dominating a bore region. In a spilling breaker, steep crests spill down the forward wave face to produce a smaller roller vortex; initially, only weak turbulence occurs within the roller, but it gradually develops into turbulent bores in the bore region.

[3] On the basis of experimental measurements by a laser Doppler velocimeter (LDV) [e.g., *Nadaoka et al.*, 1989; *Okayasu et al.*, 1986; *Ting and Kirby*, 1995, 1996] and particle imaging velocimetry (PIV) [e.g., *Chang and Liu*, 1999; *Melville et al.*, 2002], mean velocities and turbulence statistics have been described over a cross-shore vertical plane in breaking waves. By observing the motions of bubbles entrained by breaking waves, *Nadaoka et al.* [1989] found that three-dimensional organized vortex structures, involving the so-called obliquely descending eddy, trap bubbles behind primary roller vortices. Using a large-eddy simulation based on a single (water) phase approach, *Watanabe et al.* [2005] found that a strong stretch, occurring in a saddle region on a shear layer between roller vortices, changes the orientation of the primary vorticity, causing counterrotating vortices to be stretched on the shear layer. The two-dimensional array of horizontal rollers evolves into

[1]School of Engineering, Hokkaido University, Sapporo, Japan.
[2]Disaster Prevention Research Institute, Kyoto University, Kyoto, Japan.

0148-0227/08/2006JC003950$09.00

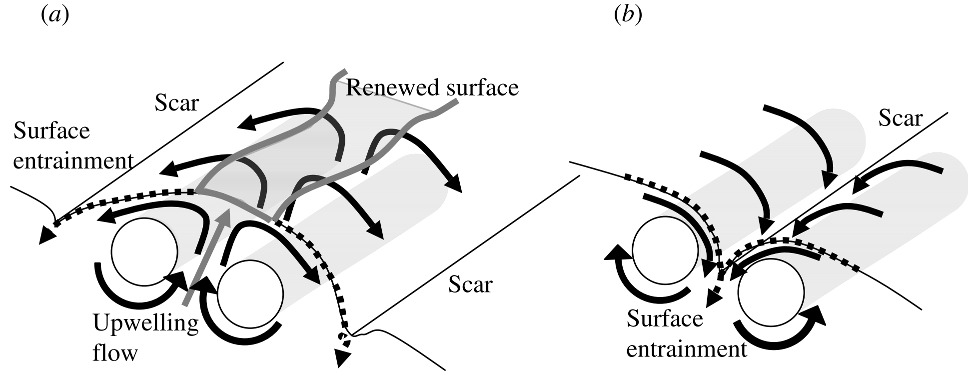

Figure 1. Surface flows and scars induced by a pair of counterrotating vortices located horizontally beneath a surface; (a) divergent surface flow and (b) convergent surface flow.

a three-dimensional structure via shear-induced counterrotating vorticity, which is aligned in the spanwise direction.

[4] Splash-up interval and wave speed determine the relative locations of rollers, as well as the initial strength of the shear between primary rollers. In turn, splash-up interval and wave speed are governed by gravity, so they may be subjected to scaling by the Froude number. Therefore, unlike freely developing turbulence, which is characterized by a Reynolds number, rollers in breaking waves contribute to a primary shear field that is dominated by gravitational splashing jets. The governing parameters, however, have not been identified for production, transport, and diffusion in breaking waves, nor have appropriate scaling laws been constructed for characterizing the wave-breaking turbulence that cascades from gravity-induced large vortices into fully developed turbulence in bores.

[5] Previous studies revealed how vortices affect surface deformation and surface flow [e.g., *Sarpkaya*, 1996]. When a vortex is produced beneath the surface in a breaking process, its rotational velocity reduces the local pressure, thereby deforming the local surface into so-called 'scars'. *Brocchini and Peregrine* [2001] defined a scar to be 'a parallel line to wave direction near the wave crest on the free-surface where fluid is entrained downward from the surface layer'. When two counterrotating vortices located horizontally beneath the surface induce upwelling flow toward the surface, the surface is lifted, forming a dome-like region over the vortices [*Sarpkaya*, 1996]; in this region, the resulting divergent surface flow replaces the surface with upwelling inner fluid (see Figure 1a). As a result of vortex-surface interactions, scars form at the edges of the vortices [*Ohring and Lugt*, 1991]. Counteracting divergent surface flows are convergent flows that form over inversely rotating vortex pairs; these flows tend to depress the surface between the vortices and can form a scar at the converging line (see Figure 1b). *Jeong and Moffat* [1992] derived an analytical solution for the flow around a counterrotating cylinder located beneath the water surface horizontally, and they explained the formation of surface cusps (scars) in low Reynolds-number flows. The surface is renewed by the presence of subsurface turbulent wakes or vortices that exchange fluid between the surface and the interior [*Komori et al.*, 1989].

[6] When the temperature of the air differs from that of the water, heat flux across the sea surface occurs through a thermal boundary layer (skin layer); the thickness of the layer is on the order of 1 mm [*Jessup*, 1995; *Jessup et al.*, 1997]. When there is a heat flux from the bulk water toward the surface, the temperature in the skin layer is below that of the bulk water; however, when downward heat flux dominates (as, for example, when the surface is heated by sunlight) then the temperature of the skin layer is above that of the bulk. If, in addition, the skin layer is disrupted by turbulence, with water beneath the layer emerging into the surface, then local distributions of surface temperature can be used as a signature for the presence of turbulence on the surface. Using infrared imaging of wave faces to measure changes in surface temperature, *Jessup et al.* [1997] studied the energy dissipated in turbulent wakes caused by ocean-breaking waves. They found that the skin-layer recovery rate is directly related to breaking wave turbulence and to the energy dissipation rate. Just as for scar formation, when nearshore breaking waves are accompanied by strong turbulence on the surface, subsurface vortices promote exchange of water between the bulk interior and the surface; this disrupts the skin layer and forces surface renewal in the waves. This suggests that, by measuring thermal signatures on the surface, we can deduce the presence of subsurface vortices. Jessup and his colleagues have also discussed the impact of wind-driven microbreaking at wave crests on the surface renewal process. They examined changes in surface temperature modulation and the size of the renewed surface in a series of laboratory experiments and observations made in the open ocean [*Jessup and Hesany*, 1996; *Siddiqui et al.*, 2001; *Zappa et al.*, 2004; *Branch and Jessup*, 2007].

[7] In our study, the surface temperatures of depth-induced breaking waves were measured by infrared imaging. The measurements were used to determine subsurface three-dimensional structures of vortices that form under both spilling and plunging waves. The measurements also allowed us to determine length and timescales for secondary counterrotating vortices. These results enabled us to identify those factors that characterize the formation and evolution of counterrotating vortices through the wave-breaking process.

[8] The current paper is composed of four sections. Following this section, the experimental setup and conditions are explained (section 2). Then we discuss the formation and evolution of subsurface counterrotating vortices, as well as the scale effects of vortices (section 3). Results are summarized in section 4. We use an appendix to examine

Table 1. Wave Conditions

Run	Breaker Type	f_0[a]	H_b[b]	d_b[c]	d_p[d]	s_f[e]	View Angle	Illumination
1	Plunging	0.54	11.0	13.7	12.0	0.349	90	Yes
2	Plunging	0.54	11.0	13.7	12.0	0.349	90	No
3	Plunging	0.54	11.0	13.7	12.0	0.349	45	Yes
4	Plunging	0.54	11.0	13.7	12.0	0.349	45	No
5	Spilling	0.90	9.8	12.8	-	0.221	90	Yes
6	Spilling	0.90	9.8	12.8	-	0.221	90	No
7	Spilling	0.90	9.8	12.8	-	0.221	45	Yes
8	Spilling	0.90	9.8	12.8	-	0.221	45	No
9	Plunging	0.25	100.2	92.0	81.3	0.333	30	Sunlight
10	Spilling	0.4	89.2	90.0	81.3	0.220	30	Sunlight

[a]Basic frequency of waves (Hertz).
[b]Breaking wave height (centimeters).
[c]Breaking water depth (centimeters).
[d]Depth at the plunging point (centimeters).
[e]Surf similarity parameter(which equals tan $\theta/\sqrt{H_b/L_0}$, where θ is bottom slope and L_0 is offshore wavelength).

how solar reflection from wave faces affects thermal measurements performed in a large open-air wave flume.

2. Experimental Setup

[9] Infrared measurements were conducted on breaking waves in a surf zone at both small and large scales; the same instruments were used in both sets of experiments. Here, we first describe those instruments, then we describe the setup used in each of the two experimental situations.

2.1. Instruments

[10] An infrared thermographic camera (Avionics TVS8500 with a temperature resolution of 0.025°C, InSb infrared detector) was set over a wave flume. The camera detects infrared rays over two spectral bands of 3.5–4.1 μm and 4.5–5.1 μm. A relation of surface temperature (T) and infrared energy (D) over the bands for a gray body with the emissivity ϵ is given by

$$D = \epsilon A T^4, \tag{1}$$

where A is the Stefan-Boltzmann constant (see a review by *Meola and Carlomagno* [2004]). Since the camera receives not only D for the water surface but also the infrared energy of ambient temperature (D') and radiation from the camera itself (D''), the following polynomial with lower order correction terms is used to estimate T from the detected total infrared energy ($D^* = D + D' + D''$) instead of (1):

$$D^* = \alpha + \epsilon\left(A_1 T + A_2 T^2 + A_3 T^3 + A_4 T^4\right). \tag{2}$$

Here α and A_n are calibration constants. The measured surface temperature (T) has contributions from both infrared radiation T_{rad} and reflection T_{ref} from the surface; however, the temperature can be properly estimated from (2) only when T is approximated by T_{rad}. Obviously, the reflective contribution to T is negligible when the surface is not illuminated (as in runs 2, 4, 6, and 8 of Table 1). To acquire visible images of wave surfaces and compare them with simultaneously measured surface temperatures, in some runs we illuminated wave surfaces with visible light.

[11] To study how the estimated temperatures were affected by surface reflection, we performed small-scale measurements at selected wave conditions both with and without visible illumination. When the surface was illuminated, an eight-bit digital video camera (Kodak ES1.0) equipped with a 50-mm focal lens (Micro Nikkor) was placed beside the thermographic camera; both cameras were

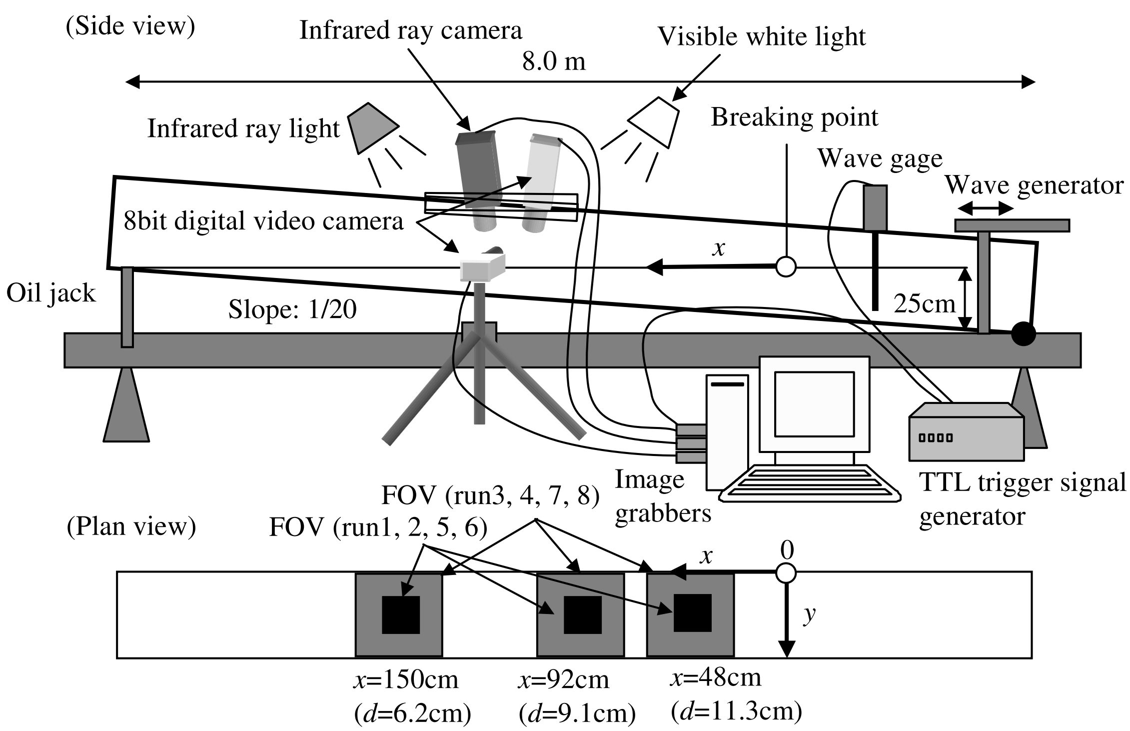

Figure 2. Experimental setup for the small-scale experiment.

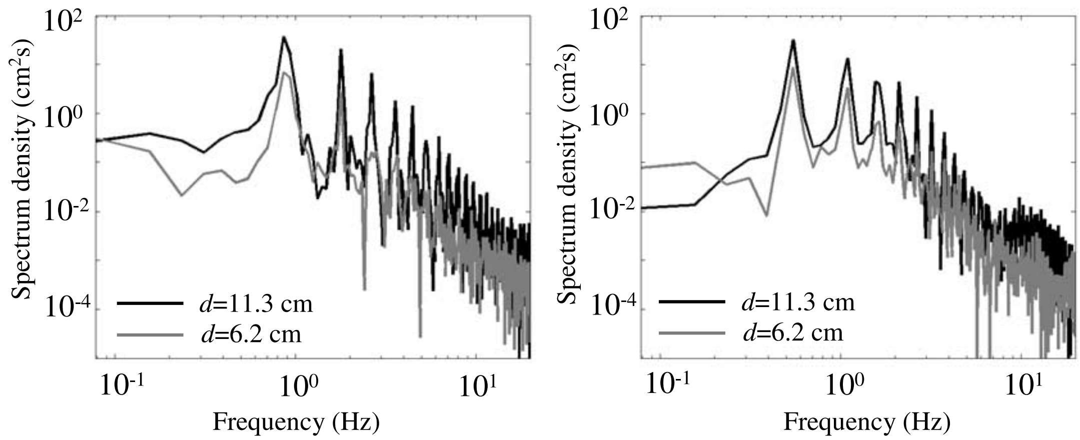

Figure 3. Incident wave spectra for (left) spilling breaker and (right) plunging breaker.

oriented to the same viewing angle, thereby providing simultaneous infrared and visible images of the wave surfaces. The infrared camera had a resolution of 236 × 256 pixels and a frame rate of 30.0 fps; the video camera had 1024 × 1024 pixels at 29.0 fps. To compensate for the difference in frame rates, images from sequential video frames were interpolated to obtain video images that were in phase with the infrared images. We found all time records for mean surface temperature, measured with illumination, to be highly correlated (in the range of 0.91–0.99) with corresponding measurements taken in the absence of visible illumination; that is, under the conditions of illumination used in the small-scale experiments, the values estimated for surface temperatures were not affected by infrared reflection.

[12] During splashing, breaking waves normally contain aerated surfaces. Because of changes in thermal capacity and thermal radiation at the surface, aeration might affect surface temperatures; however, we observed no correlation between surface temperatures and visible-image intensities on aerated surfaces (e.g., Figures 6 and 7). Therefore, we conclude that our measured surface temperatures were not directly affected by aeration in the surface.

2.2. Small-Scale Laboratory Experiments

[13] Small-scale experiments were conducted in a wave flume that was 8 m in length, 0.6 m in depth, and 0.25 m in width. The flume had transparent acrylic walls and was placed in a dark room to avoid any effects from ambient light (see Figure 2). The cross-shore coordinate (x), with its origin at the breaking point, was defined as in Figure 2. Waves were generated by a piston-type wave generator, which was set at one end of the wave flume. A hinge was set at the bottom under the wave paddle and, at the other end of the flume, an oil jack was fixed at the bottom; by adjusting the jack, we tilted the flume to create a uniform beach having a slope of 1:20.

[14] In experiments on shoaling waves, the sloping section of a wave flume is normally separated from the wave paddle by a section having constant depth; this allows experimental determinations of both incident and reflected wave heights. Because our flume did not have a constant-depth section, a reflection coefficient could not be determined directly. Instead, reflection coefficients were estimated from other studies. Reflection coefficients for broken waves were presented by *Straub et al.* [1958] over diverse wave conditions and bottom slopes. On the basis of that study, we estimate the reflection coefficient for our wave conditions (shown in Table 1) to be less than 0.02. This indicates that most incident wave energy was dissipated through wave breaking and that reflected waves (whose wave energy was only 0.04% of the incident energy) made negligible contributions to surf-zone flow. In our experiments (see Figure 3), the typical wave spectrum for a breaking wavefield was dominated by a basic frequency plus its higher harmonic components; no significant wave energies were observed at low frequencies. That is, our experimental waves periodically broke at the same point and were not accompanied by long-period oscillations in the wave flume.

[15] The video and infrared cameras were both connected to image grabbers installed in a personal computer (Pentium 4, 2.0 GHz). Image acquisition was triggered by a transistor-transistor logic (TTL) signal that was generated when a wave gage, placed in front of the wave paddle, detected the first generated wave (see Figure 2). Captured images were stored in the computer during the experiment; subsequently, they were converted to eight-bit bitmap image files. A second wave gage was set at the measurement site and was triggered by the same TTL signal that triggered the image acquisition systems. By synchronizing images and wave records at the measurement site, we simultaneously obtained values for surface temperatures, local surface deformations, and wave phases.

[16] Each camera had a field of view (FOV) of about 13.3 cm × 13.3 cm for measurements at 90° to the still water surface (runs 1, 2, 5, and 6) and about 33.3 cm × 33.3 cm for measurements at 45° (runs 3, 4, 6, and 7). Runs with the larger FOV were used to study spatial features of spanwise patterns of surface temperature over a wide area (these are discussed in sections 3.1 and 3.4). Runs with the smaller FOV (runs 2 and 6) were used to study cross-shore local changes in mean temperature (these are discussed in sections 3.2 and 3.3).

[17] Image noise was reduced by median digital filters. To calibrate image coordinates with real coordinates, a board with a square grid was set at the still water level and photographed by both cameras. To correct aberrations, we

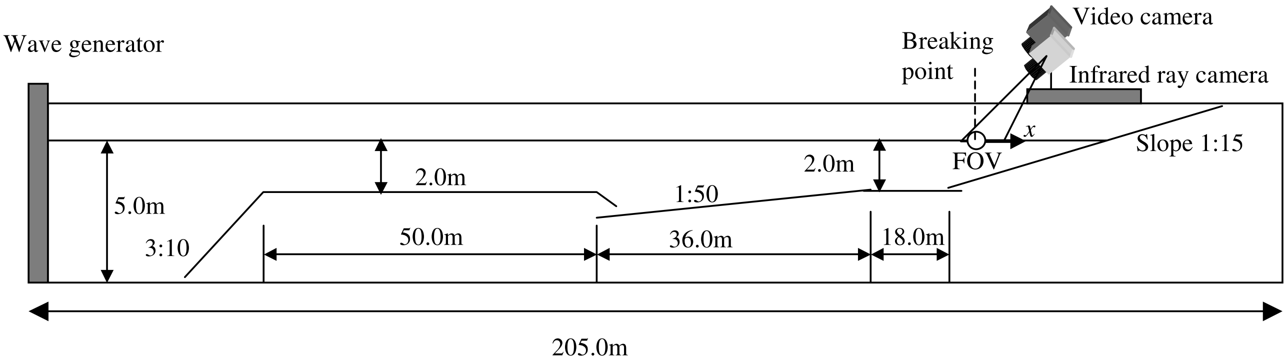

Figure 4. Experimental setup for the large-scale experiment.

transformed the coordinates from all infrared and visible images by applying a linear image projection to obtain orthogonal real coordinates at the still water level. This linear transformation may be appropriate if the wave amplitude (less than 5.5 cm) is much smaller than the optical distance to the still water level (60 cm). We confirmed that these image transformations, for both infrared and visible images, incurred maximum errors of less than 0.2%.

[18] In all runs, initial temperatures of the still water surface were controlled to be 1.3°C above bulk water temperatures. This was done, prior to starting each run, by using infrared lights to heat the whole still water surface. To eliminate any possible error associated with reflection of visible illumination, only small-scale results without illumination are used to discuss quantitative surface temperatures (see sections 3.2, 3.3, and 3.4).

[19] During a series of wind-wave experiments in a laboratory, *Zappa et al.* [2004] observed capillary waves riding on the front face of relatively short wind waves (with frequencies of 2.5–3.0 Hz). The phase speed of the capillary waves was found to be comparable with the wind waves and microbreaking was induced at the crest, enhancing the surface disruption.

[20] Surface tension may affect the evolution of a spilling breaker having a short wavelength [*Duncan*, 2001], because capillary waves generate vorticity that accumulates mainly in the gravitational wave crest [*Longuet-Higgins*, 1992]. For progressive linear waves, subjected to both surface tension and gravity, the wave speed (c) is given by

$$c = (g\lambda/2\pi + 2\pi\sigma/\rho\lambda)^{1/2}, \tag{3}$$

where g is the gravitational acceleration, ρ is the fluid density, λ is the wavelength, and σ is the surface tension. For the minimum wave speed c_m, the wavelength is estimated to be $\lambda_m = 2\pi\ (\sigma/\rho g)^{1/2} = 1.73$ cm (at 10°C). For short waves (roughly of wavelength <0.5 m), capillary ripples within waves shorter than λ_m might occur ahead of the wave crest and travel with velocities higher than or equal to the gravitational wave speed [*Duncan*, 2001]. In our small-scale experiment, capillary waves preceding the horizontal roller crest have not been observed. The incident gravitational wave speed was 0.9 m/s for spilling breakers; to have a faster wave speed, any capillary waves would need to have wavelengths estimated to be about 0.06 mm. This is much smaller than the length scale of the wave-breaking induced vortices observed in this study (1.7–3.0 cm for a spilling breaker, 5.0–8.0 cm for a plunging breaker). Therefore, there was no significant effect of capillary waves on the breaking waves chosen in the experiment. It has been also confirmed that there was no change in surface reflectivity associated with surface roughness at the crest over wave periods, comparing the cases with and without illumination for the same wave conditions.

[21] On the other hand, a series of studies on sea surface temperatures with infrared imagery by Jessup and his colleagues has revealed that wind-driven microbreaking of ocean waves has a primary role for renewing the surface owing to breaking turbulence, resulting in modulations of the surface temperature [*Jessup and Hesany*, 1996; *Jessup et al.*, 1997; *Wick and Jessup*, 1998; *Siddiqui et al.*, 2001; *Branch and Jessup*, 2007]. The temperature modulation has been observed to appear at different phases in open ocean, which is caused by microbreaking owing to short waves bounded on longer swell waves [*Branch and Jessup*, 2007]. For depth-induced breaking waves, identical turbulence in the bore is also formed in front of the wave crest to induce the temperature modulation. Typical features of the surface renewal scale and surface vorticity (section 3.1) and the resulting temperature modulation (section 3.2) for the depth-induced nearshore wave breaking are discussed through comparisons with the earlier findings.

2.3. Large-Scale Open-Air Experiments

[22] To study the scale effects of vortices in a surf zone, we compared wave surface temperatures in the small wave flume with those obtained in a large flume. Large-scale experiments were performed in an open-air flume that was 200 m in length, 6 m in depth, and 3.5 m in width; this flume allowed us to simulate high waves at prototype scale (see Figure 4). Waves were generated by a piston-type wave generator placed at one end of the flume; the waves broke over a uniform concrete slope of 1:15. Far from the slope, there was no significant undulation of incident wave height over the uneven bottom.

[23] The infrared and synchronized digital video cameras were mounted on a platform above the wave flume; both cameras were oriented to a view angle of 30° with respect to the still water surface. This provided a FOV of 3.25 m (length) × 3.0 m. Infrared- and visible-image coordinates

were linearly transformed to coincide with the real locations in the same manner as was used in the small-scale experiments. The maximum errors incurred by the image transformations were 0.5% for the visible images and 1.75% for the infrared images.

[24] In the open-air flume, the initial surface temperature depends on solar radiation intensity, which could not be fully controlled. At the measurement site, the surface temperature was about 2.5°C higher than the bulk water temperature; this was twice the initial temperature used in the small-scale experiments. *Jessup and Hesany* [1996] found that a peak-to-peak modulation of the sea surface temperature owing to microbreaking depends on a bulk-skin temperature difference. Therefore, a local amplitude of the surface temperature in the large-scale experiment is unable to be directly compared with that in the small-scale experiment. The measured temperature in the large-scale experiment is used only for studying temperature patterns on the surface and estimating length scales and timescales of fluctuations of the surface temperature in order to identify scale effects of the surface renewal in section 3.4.

[25] In our small-scale experiments we confirmed that measured surface temperatures were not affected by surface reflection; however, sunlight contains a high-intensity spectrum in the infrared band and, consequently, temperatures measured in the large-scale experiment were affected by surface reflection. These effects are examined quantitatively in the Appendix. The uncertain surface temperatures influenced by solar reflection have been eliminated from the original measured results.

2.4. Wave Conditions

[26] Table 1 shows the breaking-wave conditions used in both the small-scale and large-scale experiments. To estimate scale effects (discussed in section 3.4), we performed some small- and large-scale measurements at the same value for the surf similarity parameter (S_f),

$$S_f = \frac{\tan\theta}{\sqrt{H_b/L_0}}. \qquad (4)$$

Here θ is the slope of the bottom, H_b is the breaking wave height, and L_0 is the offshore wavelength. Matching values for S_f ensured that we attained the same breaker type and breaking process in each pair of runs: for plunging waves we used $S_f \approx 0.34$ in run 4 at small scale and run 9 at large scale; for spilling waves we used $S_f = 0.22$ in run 8 at small scale and run 10 at large scale. In the small-scale experiments, the measurements were performed at four water depths: d = 11.3, 9.1, 8.3 and 6.2 cm. For a plunging breaker (runs 1–4), a shoaling wave crest overturns and plunges into the forward water in the breaking region (d = 11.3 cm), and the secondary jets repeatedly splash on the surface in the plunging (or transition) region (d = 9.1 cm) until the wave-breaking front evolves into the turbulent bore preceding the wave crest in the bore region (d = 8.3 and 6.2 cm). For a spilling breaker (runs 5–8), a weak roller vortex is formed at the spilling wave crest in the spilling (or transition) region (d = 11.3 and 9.1 cm) and it also becomes the turbulent bore in the bore region (d = 8.3 and 6.2 cm). In the large-scale experiments, the measurements were performed at d = 89 cm (plunging region for run 9, and spilling region for run 10).

3. Results

[27] We divide the discussion of results into four parts: patterns of surface temperature (section 3.1), transitions of surface temperature (section 3.2), turbulent thermal diffusion (section 3.3), and scaling laws for counterrotating vortices (section 3.4).

3.1. Patterns of Surface Temperature on Breaking Waves

[28] In section 1 we discussed how surface temperatures change when water moves between the surface and the bulk interior; such exchanges of water result when subsurface vortices are created by breaking waves. The typical patterns of surface temperatures and its relation with the counterrotating vorticity formed in breaking waves are discussed in this section.

[29] Surface temperatures and the simultaneous visible images are shown in Figure 5 for data taken from a plunging breaker: run 3 in the small-scale experiment, measured at a depth in the breaking region of d = 11.3 cm. Figure 5 shows no change in surface temperature as waves pass the measurement site seaward of the plunging point because there is no disturbance to disrupt the skin layer. Shoreward of the plunging point and after a wavefront has passed, however, several patches of low temperature can be seen; those patches extend longitudinally in the direction opposite to that of wave propagation but they are disrupted at the next onset of breaking waves (see Figure 6).

[30] Aeration may affect our estimated surface temperatures because values for thermal capacity and reflection index in air differ from those in water. The presence of cold-water patches, however, can be confirmed by comparing infrared images to simultaneous visible images; in such comparisons, cold-water patches clearly appear after an aerated wave face has passed the site. This indicates that aeration does not influence the emergence of cold water on the surface.

[31] In the large-scale experiments, identical patterns of surface temperature were observed at the plunging point; however, there was no signature at corresponding regions in the simultaneous visible images (see Figure 7). For both small- and large-scale experiments, these patterns of surface temperature commonly have an organized structure aligned in the spanwise direction at a certain interval. In addition, the formation of cold patches may be driven by the same mechanism that causes the initial entrainment of air bubbles. Evidence for this conjecture comes from both laboratory and in situ observations [see *Nadaoka et al.*, 1989, Figure 9] in which spanwise structures, analogous to those described here, were observed to organically aerate behind the wave crest line.

[32] When turbulent wakes are produced by wind wave breaking, *Jessup* [1995] and *Jessup et al.* [1997] found that surface regions form at temperatures above that of the surrounding area; such regions form a warm patch that extends behind the whitecap. In these situations, a net upward heat flux may form a skin layer on the ocean surface; the skin would be at a higher temperature than

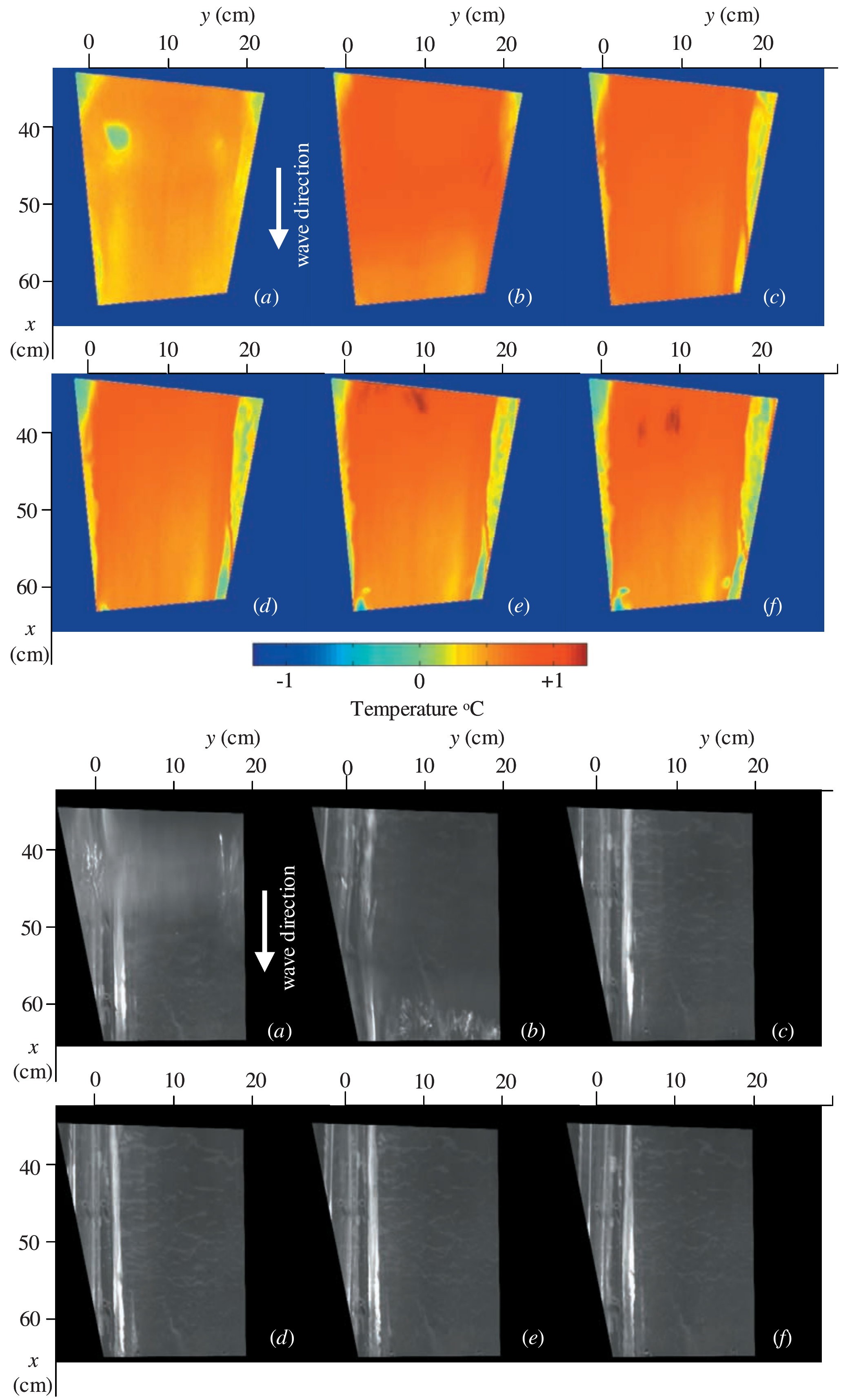

Figure 5. (top) Sequential surface temperatures relative to the mean bulk-water temperature (12.1°C) and (bottom) simultaneous visible images at $d = 11.3$ cm (breaking region) in run 3 (plunging breaker) of small-scale experiments. Phases a–f are successive phases at 0.2-s intervals.

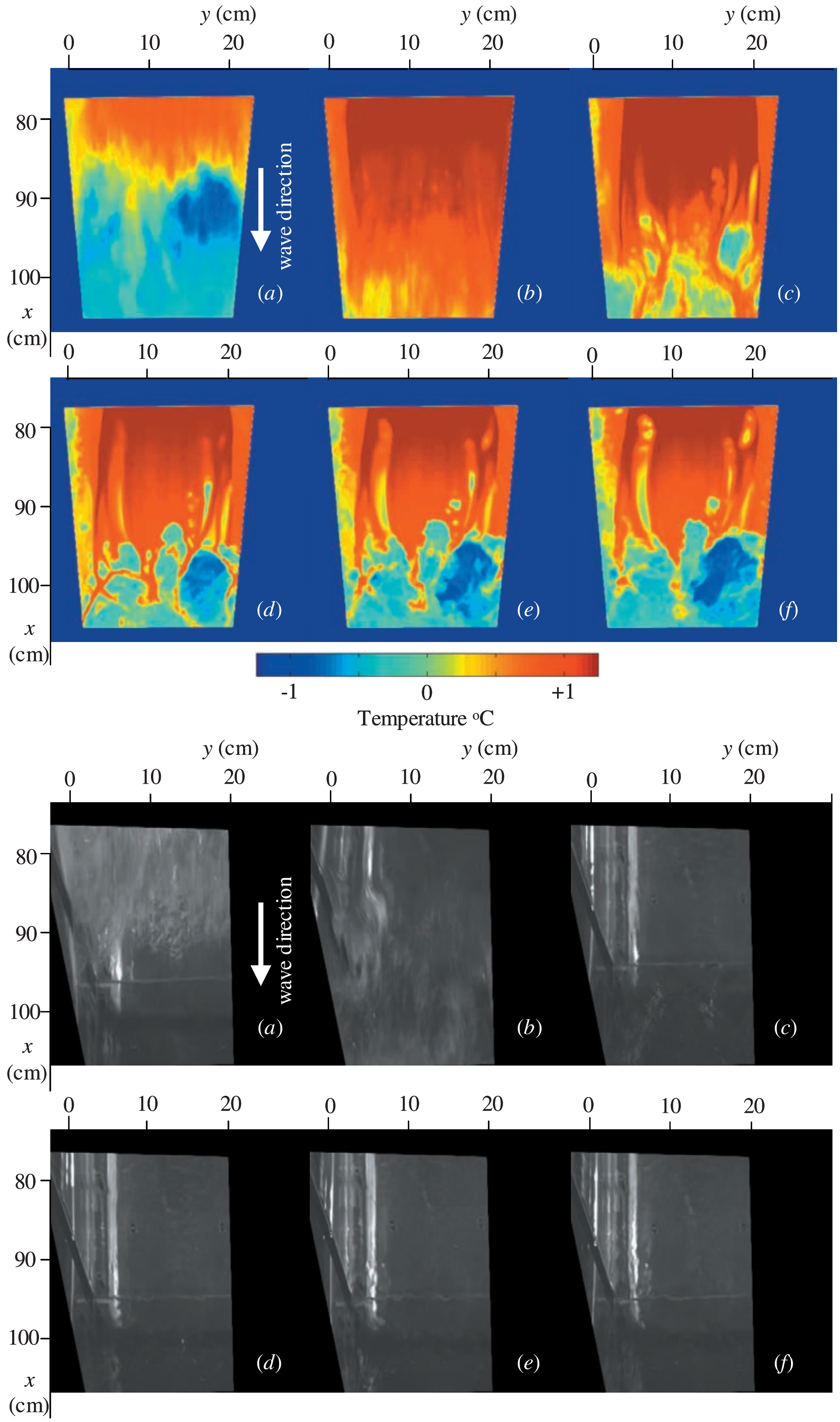

Figure 6. (top) Sequential surface temperatures relative to the mean bulk-water temperature (11.5°C) and (bottom) simultaneous visible images at d = 9.1 cm (plunging region) in run 3 (plunging breaker) of small-scale experiments. Phases a–f are successive phases at 0.2-s intervals.

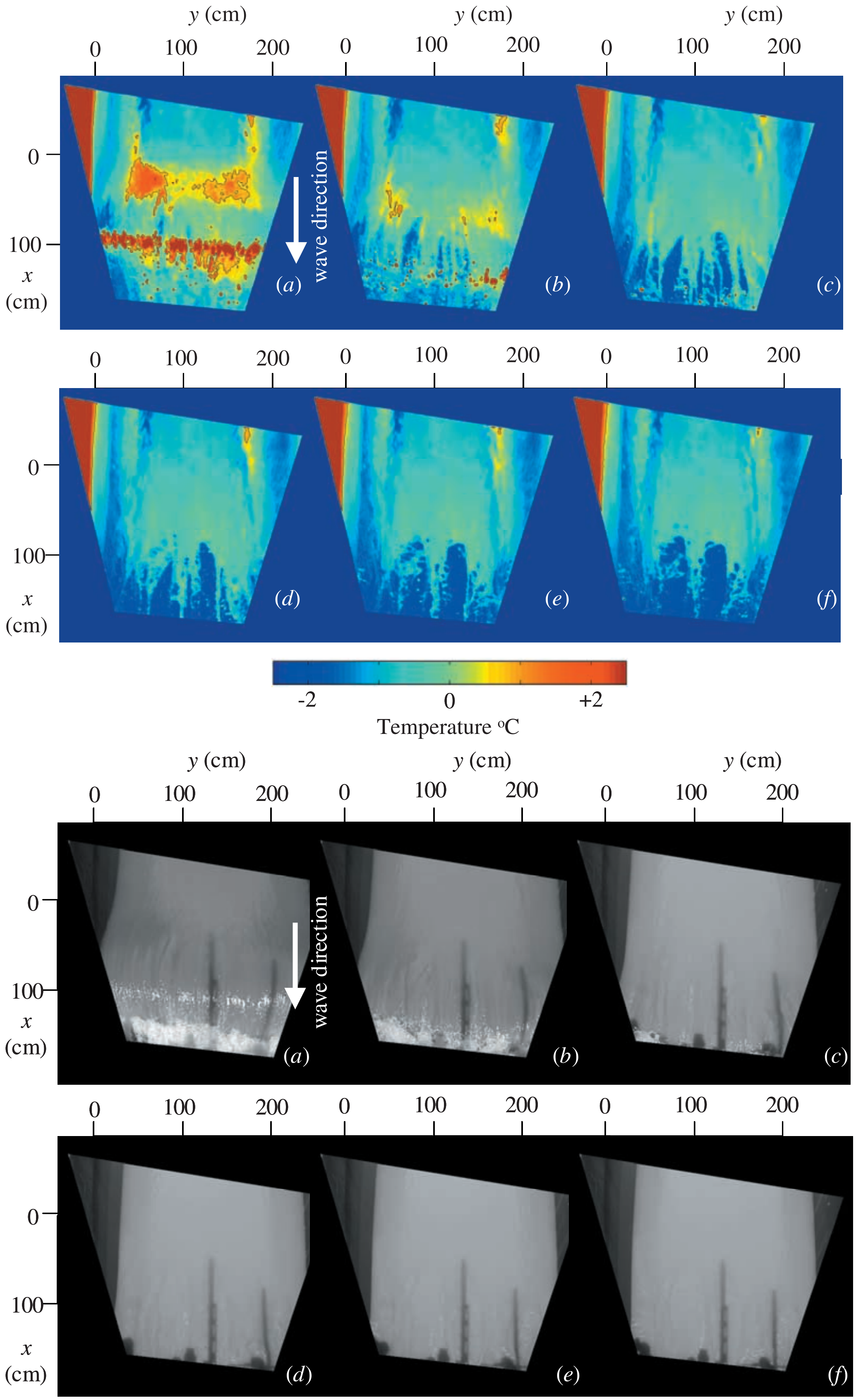

Figure 7. (top) Sequential surface temperatures relative to the mean temperature (12.5°C) and (bottom) simultaneous visible images at d = 89.0 cm (plunging region) in run 9 (plunging breaker) of large-scale experiments. Phases a–f are successive phases at 0.2-s intervals. The surface area significantly affected by solar reflection is surrounded by a solid line (see Appendix A).

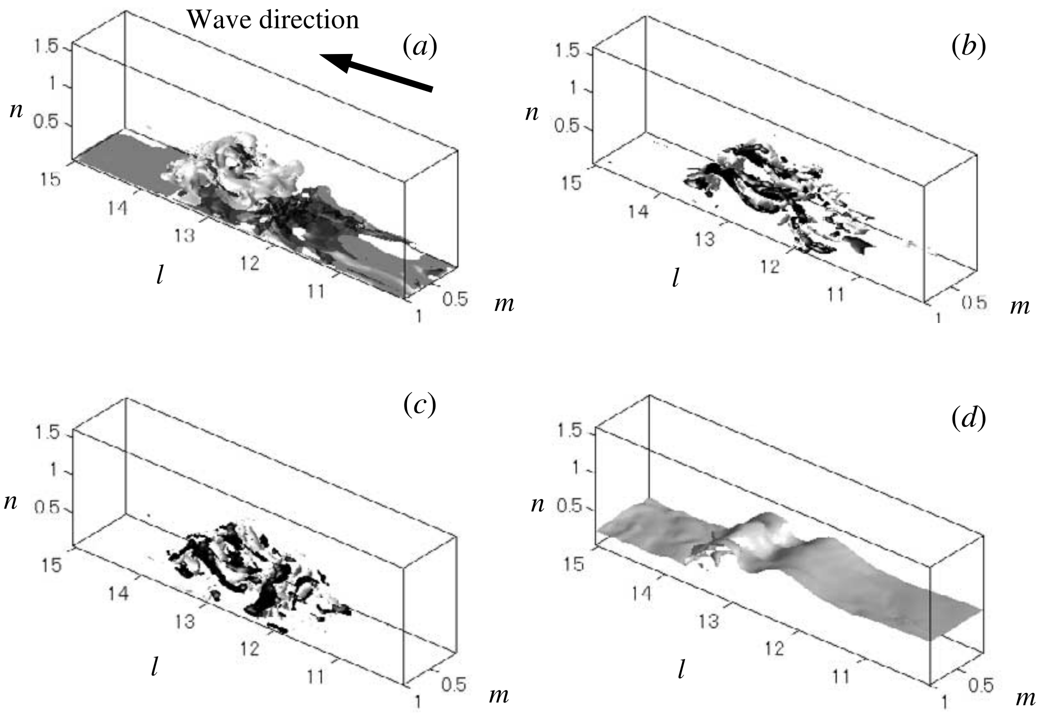

Figure 8. Typical surfaces of constant vorticity in breaking waves. (a) Spanwise vorticity, (b) streamwise vorticity, (c) vertical vorticity, and (d) waveshape [after *Watanabe et al.*, 2005].

the bulk underneath, and therefore when surface turbulence disrupts the skin, the result would be the formation of warm patches on the surface. In our experiments, patches and undisturbed surface had relative temperatures that were the opposite of those in field measurements because, in our experiments, there was a downward heat flux across the water surface: we controlled the surface temperature of the initial still water to be 1.3°C higher than the bulk temperature.

[33] From deep-water field measurements, *Jessup* [1995] found a linear or quadratic relation between wake length in the direction of propagation and wave crest speed. In our large-scale experiments (runs 9 and 10), patch lengths were in the range of 2.2–2.8 m for a wave speed of 2.87 m/s; these are within the range of Jessup's 2.3–4.4 m and are roughly consistent with the measured turbulence signatures of in situ breaking waves.

[34] In our small experiments, however, the patch lengths were about 0.2 m at a wave speed of 1.25 m/s (run 2); this deviates from the 1.2–2.0 m estimated from *Jessup*'s [1995] wake-length relation for the corresponding wave speed. Breaking-wave height should also contribute to the initial intensity of turbulence that is produced from the vortex created by an overturning jet. Therefore, the inconsistent turbulent wake lengths might be explained by the considerable difference in breaking-wave heights between our small-scale experiment and Jessup's in situ measurements. This scale effect is discussed in section 3.4.

[35] From large-eddy simulations of surf-zone breaking waves, *Watanabe et al.* [2005] found that strong shear forms between a secondary jet and a horizontal roller behind it; this reorients the vorticity and produces a counterrotating vorticity aligned parallel to the spanwise direction (see Figure 8). These vorticities are stretched on the shear layer, which extends obliquely down from the secondary jet to the bottom of the roller vortex, and they develop longitudinally beneath the free surface. These counterrotating vortices appear to partially renew the free surface and thereby create organized patterns of surface temperature [*Jeong and Moffat*, 1992; *Komori et al.*, 1989].

[36] Figure 9 illustrates surface entrainment into the inner bulk water and surface renewal caused by longitudinal counterrotating vortices that form behind a breaking wave crest. Depending on their rotation, a single pair of counterrotating vortices may induce either divergent or convergent flow on the surface above (see section 1 and Figure 1); but

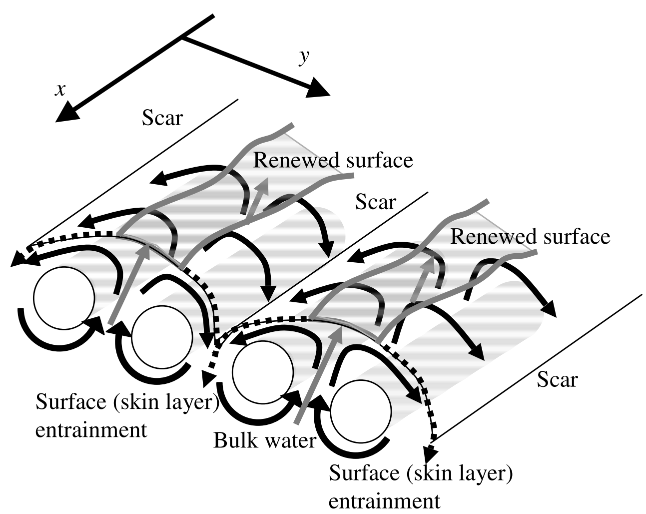

Figure 9. Surface renewal and surface entrainment caused by multiple pairs of subsurface counterrotating vortices.

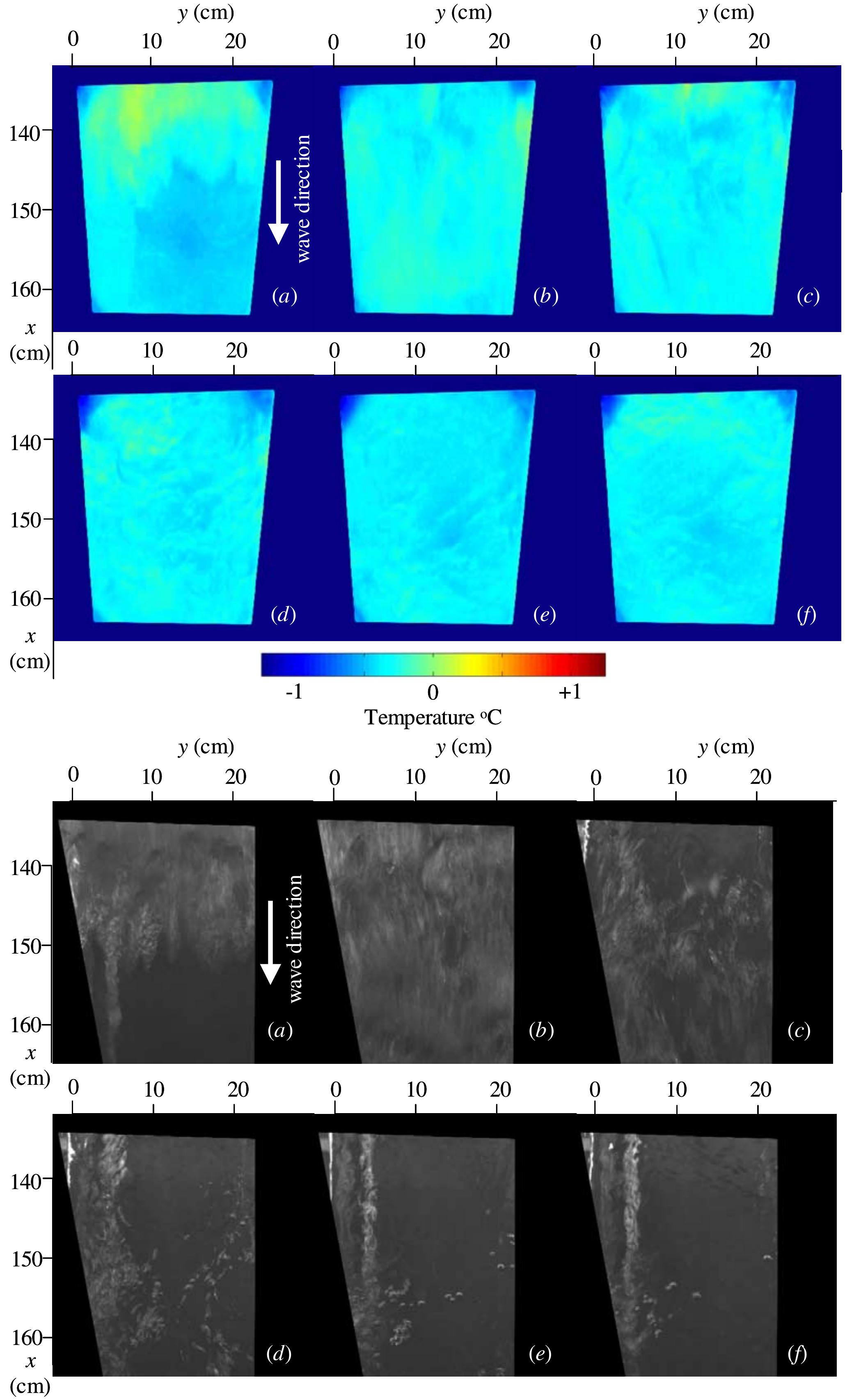

Figure 10. (top) Sequential surface temperatures relative to the mean bulk-water temperature (12.0°C) and (bottom) simultaneous visible images at d = 8.3 cm (bore region) in run 3 (plunging breaker) of small-scale experiments. Phases a–f are successive phases at 0.2-s intervals.

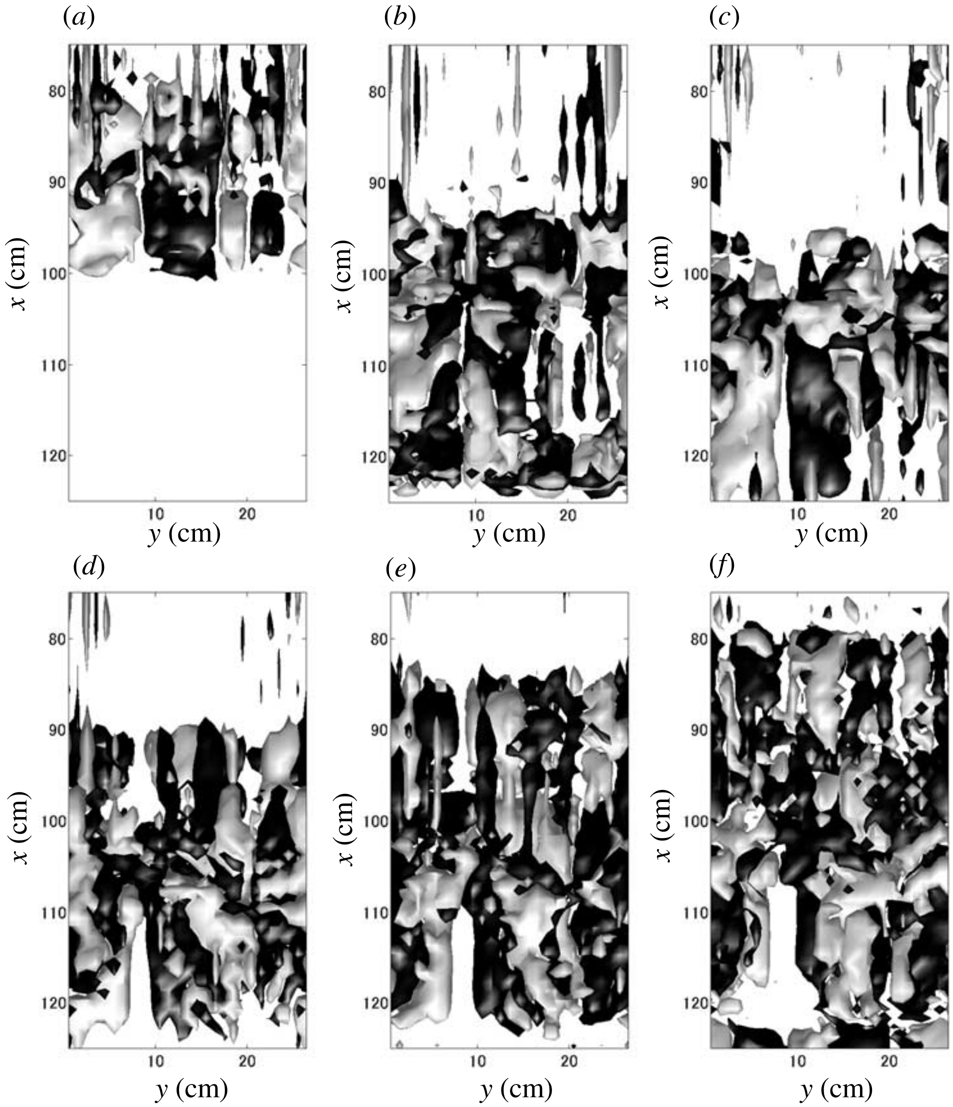

Figure 11. Plan view of surfaces of constant streamwise vorticity for run 3 (plunging breaker), computed using the same large-eddy simulation as *Watanabe et al.* [2005]. Phases a–f correspond to those in Figure 6.

over an array of multiple vortex pairs, both flows alternately appear along the perpendicular to the vortex axis. Between adjacent subsurface counterrotating vortices, downward rotating flow converges and entrains the surface skin, while upwelling flow around vortices disrupts the skin to push cold inner water onto the surface.

[37] In a bore region where splashing culminates in a turbulent bore, strong small-scale turbulence first disturbs the skin layer and then enhances turbulent thermal diffusion in the whole bore. This reduces both the mean temperature and any local temperature gradients on the surface (see Figure 10).

[38] Sequential plan views of surfaces of constant streamwise vorticity ($\partial v/\partial z - \partial w/\partial y$) are shown in Figure 11 for the six phases appearing in the infrared images of Figure 6; the constant-vorticity surfaces in breaking waves were computed from incident wave data in run 3 using the same method as *Watanabe et al.* [2005]. After passing the breaking wavefront, three major pairs of counterrotating vorticities formed (see Figure 11, phase c); these vorticities gradually moved offshore and at the same time deformed in complicated ways (see Figure 11, phases d–f). These computed vorticity distributions are consistent with the locations and regions where cold bulk water emerges onto the surface (attributed to subsurface vortices of successive phases), as shown in Figure 6.

[39] Figure 12 shows computed distributions of absolute streamwise vorticity averaged over the spanwise y axis on a horizontal-vertical (x-z) plane. When an overturning jet plunges in front of a wave, the mean streamwise vorticity appears 2–5 cm below the surface of the jet (see Figure 12, phases a and b). At this stage, the free-surface has not been disturbed nor renewed because no significant vorticity has yet formed near the surface; therefore, in Figure 6, the (almost) uniformly high temperatures, which indicate an undisturbed surface, appear on the wave surface at phases a

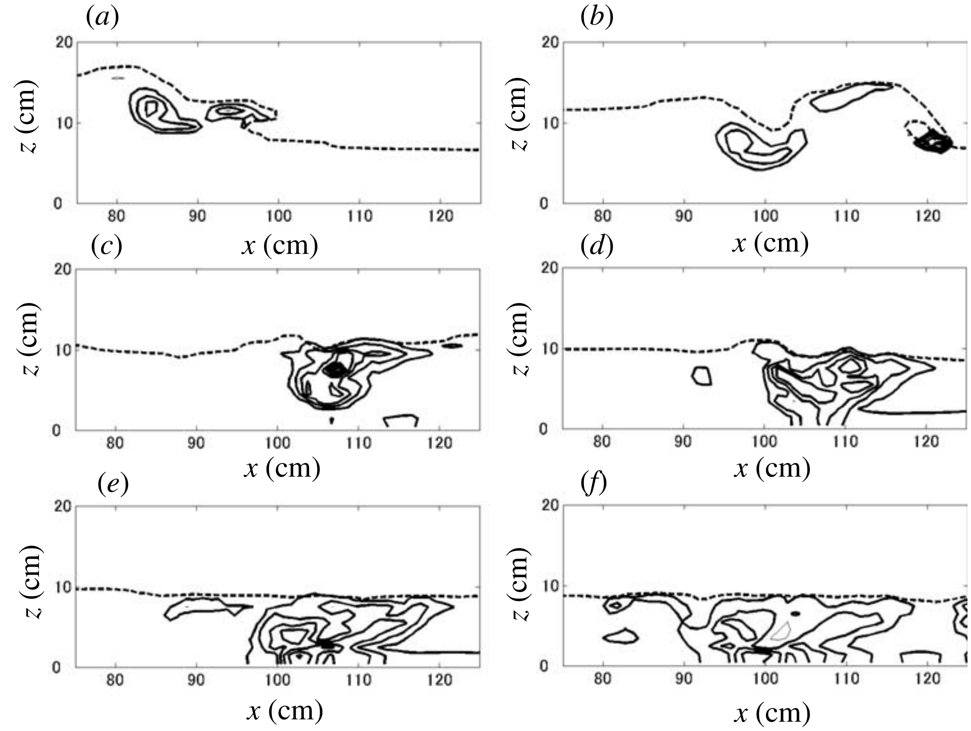

Figure 12. Cross-sectional distributions of the computed streamwise vorticity (rms) averaged over the spanwise direction for run 3. Contour interval: $\pi/2\ s^{-1}$. Phases a–f correspond to those in Figure 6.

and b. Consequently, surface renewal is not affected by the counterrotating vortices that appear at x = 80–90 cm in Figure 11 (phase a) or at x = 95–105 cm in Figure 11 (phase b). We note that, while the observed temperature pattern, a clear gradient around $x \sim 90$ cm in Figure 6 (phase a), is consistent with the vortical distribution in Figures 11 and 12 (phase a), the numerical wavefront propagates faster than the observed one. The strong turbulence produced after wave breaking generally alters the local waveshape and the local flow in the surf zone every breaking onset, while the identical regular waveform is periodically observed in the location prior to breaking [*Cox and Kobayashi*, 2000]. The discrepancy of the instantaneous speed of the computed and observed wavefronts may pertain to the uncertainty of velocity field in the both experimental and computational surf zone. A statistical description may be needed to identify the measured and computed results, which remains to be studied.

[40] After the breaking wave has passed (see Figure 12, phases c and d), however, a significant vorticity is induced on the surface; this vorticity disturbs and renews the surface in the region near x = 100–115 cm and creates the low-temperature patches that appear in Figure 6. As shown in Figures 11 and 12 (phases e and f), the counterrotating vortices move offshore, but remain near the surface to create the longitudinal patterns of surface temperature seen in Figure 6. The large temperature gradient at x = 95 cm in Figure 6 (phases e and f) locates a boundary between surfaces with and without significant vorticity (see Figure 12). As the vortices continue to move offshore, surface renewal continues and the size of the renewed surface continues to spread until the surface is covered by the next onset of breaking waves. From these rough comparisons of computed and measured results for a single case, we cannot extract the precise threshold of surface vorticity that is required to renew the surface; however, turbulent thermal diffusion on the surface (see section 3.3) provides some guidance as to how surface temperatures are affected by the cross-shore distribution of surface turbulence.

[41] The spanwise wave number spectrum is shown in Figure 13 for the streamwise vorticity computed at the wave trough level of the plunging point (x = 90 cm) for each phase in Figure 11. For splashing phase a, Figure 13 shows a relatively high wave number ($\log_{10}(k) = 1.5$) for the spectrum at the plunging point; however, no significant spectrum appears for phase b because major parts of the vortices have already passed the plunging point and are being transported toward shore (see also Figures 11 and 12). For phases c–e, Figure 13 shows a dominant vorticity spectrum developing at $\log_{10}(k)$ = 1.2 (corresponding to a spanwise wavelength of

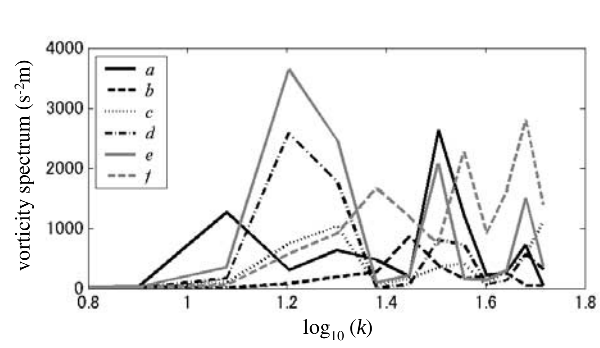

Figure 13. Computed streamwise vorticity spectra at the wave trough level of the plunging point (d = 9.1 cm) for run 3. Phases a–f correspond to those in Figures 6 and 11.

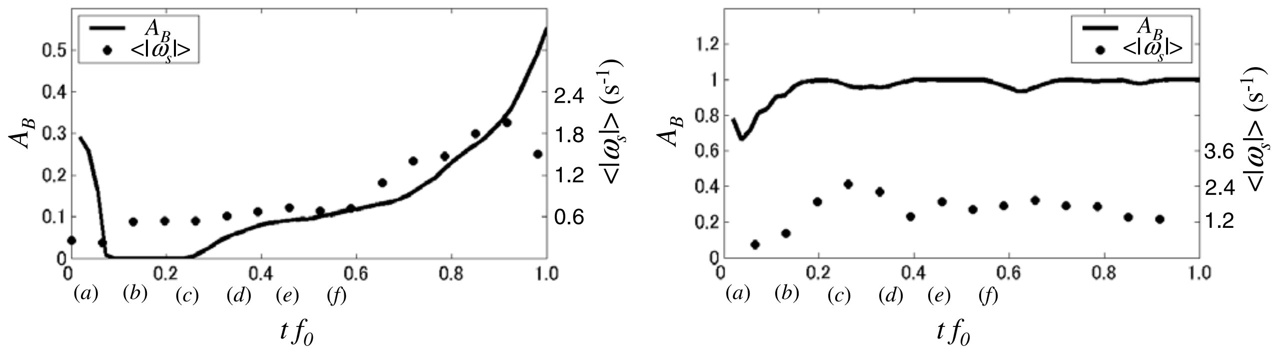

Figure 14. Time variations of the fractional area coverage (A_B) and computed streamwise vorticity (rms) averaged over 20-cm-square surface at d = 9.1 cm (left, plunging region) and 8.3 cm (right, bore region) for run 3. Phases a–f correspond to those in Figures 6, 11, and 12.

6.3 cm) and at its harmonic $\log_{10}(k)$ = 1.5 (wavelength of 3.16 cm); these phases correspond to those found experimentally in Figure 6 in which a thermal pattern extends longitudinally over the surface. A relative length of the spectrum peak 6.3 cm to the local wave height 7.0 cm was estimated to be 0.9; the spanwise intervals of counterrotating vortices were comparable to the local wave height in this region. A rough estimate of the intervals between cold patches agreed with computed wavelengths; moreover, the dominant vorticity spectrum in $1.2 \leq \log_{10}(k) \leq 1.5$ agrees with the temperature spectrum shown in Figure 20. These results demonstrate that surface renewal through disruption of the skin layer is caused by counterrotating streamwise vortices beneath the free surface.

[42] *Siddiqui et al.* [2001] found that fractional area coverage of the renewed surface highly correlates with subsurface vorticity formed behind the breaking wave crest in simultaneous measurements of the surface temperatures and velocity distribution for wind wave breaking. Using the same method as *Siddiqui et al.* [2001], the fractional area coverage (A_B) was estimated for finding any relation with the root-mean square of the computed counterrotating vorticity $\langle|\omega_s|\rangle$ near the surface (see Figure 14). In the plunging region, A_B increases exponentially to the maximum value of 0.55 after the phase c when the surface begins to be partially renewed along the vortices (see also Figure 6c) until it rapidly decreases to 0 at the recovery phase a. The rms surface vorticity $\langle|\omega_s|\rangle$ also gradually increases to 2.0 s^{-1} in analogy with A_B in the renewal term from the phase d. In contrast, in the bore region, the renewed surface fully covers the whole surface after the wavefront temporally recovers the surface at the phase a since significant vorticity, more than twice $\langle|\omega_s|\rangle$ of the plunging region, disturbs extensively the surface over a long duration. The high temporal correlations between A_B and $\langle|\omega_s|\rangle$ in the both of plunging and bore regions are consistent with the former work by *Siddiqui et al.* [2001].

[43] To summarize, changes in skin-layer temperature signal the presence of subsurface counterrotating vortices that form longitudinally under breaking waves; those vortices leave footprints that can be tracked by measuring surface temperatures. The counterrotating vorticity and its distribution on the surface determine the surface renewal scales and area coverage of the renewed surface.

3.2. Transitions of Surface Temperature

[44] In this section we discuss transitions in surface temperatures that occur by surface renewal or as a result of surface recovery following propagation of breaking waves. Consider Figure 15, which shows the following quantities at the plunging point (depth d = 9.1 cm) in run 2 (plunging breaker): surface elevation, surface temperature averaged over the measurement region, and the standard deviation of temperatures from their average. Although disruption of the skin layer decreases the surface temperature in response to development of subsurface vortices, the temperature is periodically restored at an interval corresponding to the basic wave frequency. Successive onsets of breaking waves enhance turbulent thermal mixing and gradually decrease the mean surface temperature so that it approaches the bulk water temperature. Figure 15 shows that the standard deviation for the spatial distribution of surface temperatures is not only high, but also fluctuating, apparently at the basic wave

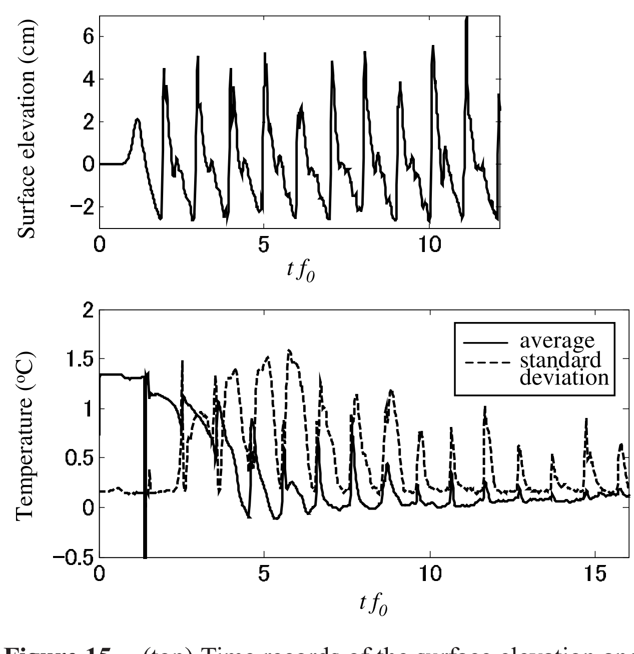

Figure 15. (top) Time records of the surface elevation and (bottom) surface temperature relative to the mean bulk-water temperature (12.0 °C) at d = 9.1 cm (plunging point) in run 2 (plunging breaker).

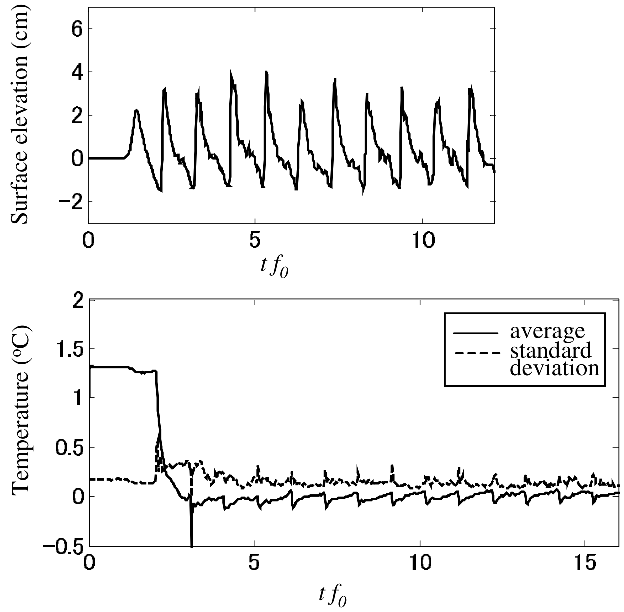

Figure 16. (top) Time records of the surface elevation and (bottom) surface temperature relative to the mean bulk-water temperature (12.0 °C) at d = 6.2 cm (bore region) in run 6 (spilling breaker).

frequency; this further suggests that a periodic disruption-restoration process (or equivalently, a surface renewal-recovery process) occurs in the skin layer. In the bore region (shown in Figures 10 and 16), strong turbulence first disturbs the surface and then disrupts the skin layer, causing the surface temperature to decrease rapidly toward the bulk temperature. Figure 16 shows that, after the first breaking wave passes the bore, average surface temperatures have smaller standard deviations than appear in Figure 15 for plunging breakers. Moreover, temperatures in the plunging region (Figure 15) behave unlike those in the bore region (Figure 16).

[45] In the plunging region (Figure 15), the average temperature exhibits a sawtooth-like variation, with the standard deviation quickly increasing to a maximum; that high standard deviation continues until the average surface temperature itself nearly reaches the bulk value. In the bore region (Figure 16), however, the standard deviation pulsates only over a short duration during which the surface temperature rapidly falls from its initial value to the bulk value. These differences are caused by qualitative differences in the surface renewal process that accompanies propagation of breaking waves.

[46] In the plunging region, the mean surface temperature gradually falls as cooler water emerges into the surface from the interior (see section 3.1). As vortices develop, renewed surfaces gradually spread on the rear face of breaking waves, leading to large variations in surface temperatures (hence, high standard deviations about the average) that extend over relatively long durations (see also Figure 6). The phase showing the maximum standard deviation delays for 0.18s (normalized time of $0.1tf_0$, f_0: incident wave frequency) from the maximum surface elevation, while the maximum temperature appears at 0.74 s ($0.4tf_0$) earlier than the maximum surface elevation phase, since the undisturbed surface of the jet projecting from breaking waves recovers the surface temperature before arriving the wave crest. In contrast, in the bore region, the recovered surface is rapidly disturbed and renewed by strong, small-scale, turbulence on the bore progressing ahead of the wave crest; in addition, the partially renewed surface is carried shoreward with the bore (see also Figure 10). Consequently, surface temperatures exhibit small fluctuations (hence, weak pulsations in the standard deviation) that extend only over the short duration of about 0.08 s ($0.07tf_0$), needed for the bore to pass the measurement site, at 0.28s ($0.25tf_0$) earlier than the maximum surface elevation. This phase opposition between the mean temperature and standard deviation in the plunging and bore regions indicates that underlying mechanisms for surface renewal change with the propagation of breaking waves. *Jessup and Hesany* [1996] observed the maximum modulation occurs on a forward face of ocean swell in the case of wind and swell aligned. On the other hand, *Branch and Jessup* [2007] found the opposite phase modulations in both laboratory and ocean observations; the surface disruption occurs on the rear face of breaking waves. This phase discrepancy of the temperature modulation is related with a relative location between microbreaking and wave crest. The temperature modulation in the plunging region (Figure 15), showing the surface is renewed on the rear face of waves, is consistent with the laboratory experiments of *Branch and Jessup* [2007]. In the bore region, the bore front precedes the wave crest to disturb the forward surface, and therefore, the surface temperature rapidly decreases and the standard deviation pulsates earlier than the maximum surface elevation phase (see Figure 16). To summarize these results, in the initial stage of breaking process, the surface renewal mainly occurs on the rear face of waves owing to the vortices left from breaking waves, while the turbulent bore preceding the wave crest disturbs the whole forward surface to renew before the wave crest arrives, resulting in a phase shift of the temperature modulation through the propagation of breaking waves.

[47] We found no significant quantitative differences between the variations of surface temperature and its standard deviation in the bore regions of spilling as opposed to plunging breakers. Sawtooth-like temperature variations were observed in the early stages of wave breaking in both spilling and plunging breakers; however, spilling breakers had high standard deviations in temperature over durations that were much smaller than those observed for plunging

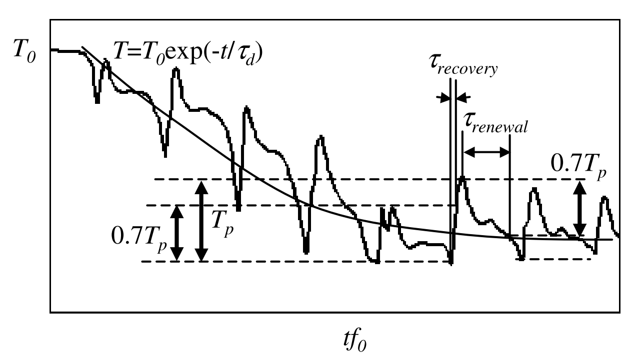

Figure 17. Timescales of surface renewal, surface recovery, and thermal diffusion.

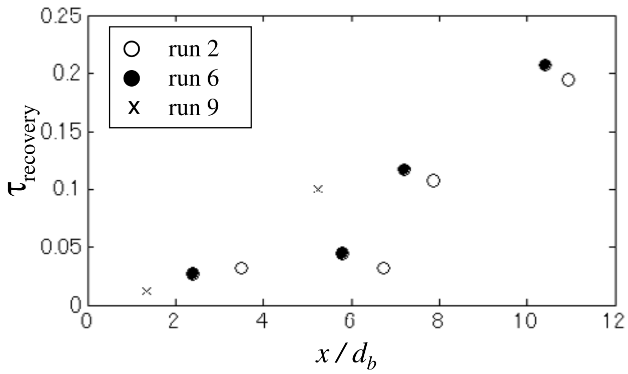

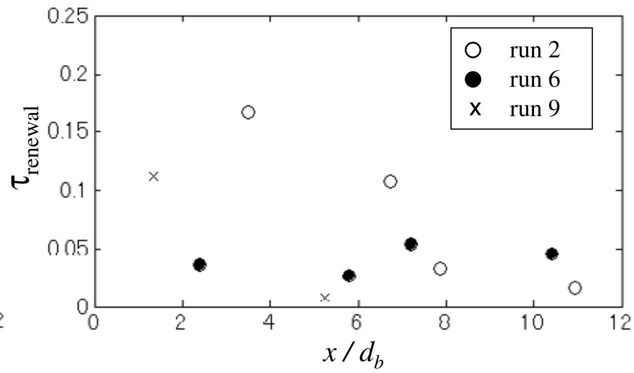

Figure 18. (left) Evolution of the dimensionless recovery and (right) renewal timescales for plunging (run 2) and spilling (run 6) breakers in small-scale experiments and for a plunging breaker in large-scale experiments (run 9).

waves. These differences in timescales are discussed later in this section. Besides differences in timescales, the two kinds of breakers differed in the rates at which the mean surface temperatures decreased to the bulk value. These differences are considered in section 3.3.

[48] Temporal variations in surface renewal and surface recovery were studied by assigning timescales to each using the methods of *Jessup et al.* [1997]. Let T_p be the range between the local minimum and maximum temperatures. Then, define the recovery timescale to be the time from the minimum peak temperature to the point at which the temperature has regained $0.7T_p$; however, rather than follow the actual oscillating temperature profile, use the time-averaged profile which exponentially decays as illustrated in Figure 17. From infrared measurements in an open ocean, *Jessup et al.* [1997] found a linear relation between the dimensional recovery timescale and the wave crest speed. For our large-scale experiment (run 9: wave speed of 2.87 m/s), we estimate the recovery time (τ_1) to be 0.4s, which agrees with Jessup's linear relation for deep-water waves. For our small-scale experiments (wave speed of 1.256 m/s for run 2, 0.90 m/s for run 6), however, the timescale was between 0.05 and 0.08 s, which deviates from the linear relation.

[49] We normalize the recovery times using the incident wave frequency f_0 ($\tau_{recovery} = \tau_1 f_0$); our normalized recovery times are shown at the left in Figure 18 for both small- and large-scale experiments. In all cases, we find that the dimensionless recovery times simply increase with the propagation of breaking waves; that is, the recovery of the skin layer becomes slower as the wave-breaking process advances.

[50] We adopt the same approach for renewal times: define the renewal timescale (τ_2) to be the time from a local maximum temperature to the point at which the temperature has decreased to $0.7T_p$; again we assume a quasi steady state profile in which the temperature falls exponentially (see Figure 17). Then we apply the incident wave frequency to make the renewal time dimensionless: $\tau_{renewal} = \tau_2 f_0$. Results are shown on the right in Figure 18. There we see that surface renewal accelerates as a plunging breaker propagates (run 2), but in a spilling breaker, surface renewal remains fast throughout the surf zone (run 6).

[51] Because renewal time depends on subsurface turbulent intensity [*Komori et al.*, 1989], the renewal process in breaking waves must also depend on turbulence, as well as on breaker type. In situations where $\tau_{renewal} < \tau_{recovery}$ (in the specific case for $x/d_b \geq 6{-}7$), surface renewal occurs more quickly than surface recovery, so the surface temperature reaches the bulk temperature by being well mixed with bulk water.

3.3. Turbulent Thermal Diffusion on the Surface

[52] Gas-transfer velocities at the air-sea interface have been studied; see *Jähne and Haußecker* [1998] for a review. The instantaneous and local gas-transfer velocities of wind waves have been estimated using an infrared imaging technique, the so-called controlled flux technique (CFT), which is based on relations among heat transfer rates, gas-transfer velocities, and Schmidt numbers [*Haußecker et al.*, 1995].

[53] The amplitude of the temperature oscillations appears to decay exponentially, as in Figure 15. Thus, the mean heat-transfer velocity and thermal diffusion on a surface can be estimated in a manner similar to that used for evaluating air-sea gas transfer. For an exponential decay of surface temperature, the turbulent thermal transfer velocity v_d may be written as

$$v_d = a\sqrt{D_T/\tau_d}, \tag{5}$$

where D_T is the turbulent thermal diffusivity, τ_d is a characteristic timescale for temperature decay, and a is a dimensionless constant [*Asher et al.*, 2004]. The timescale

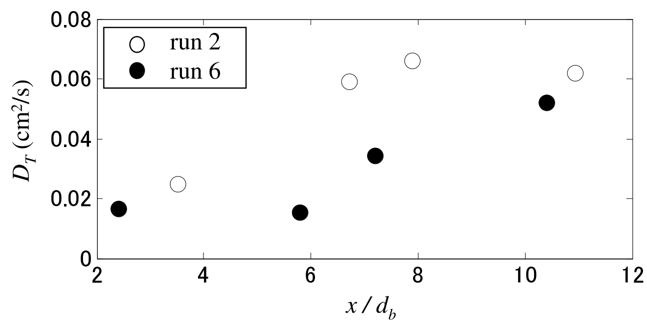

Figure 19. Cross-shore distributions of turbulent thermal diffusivity for plunging (run 2) and spilling (run 6) breakers in small-scale experiments.

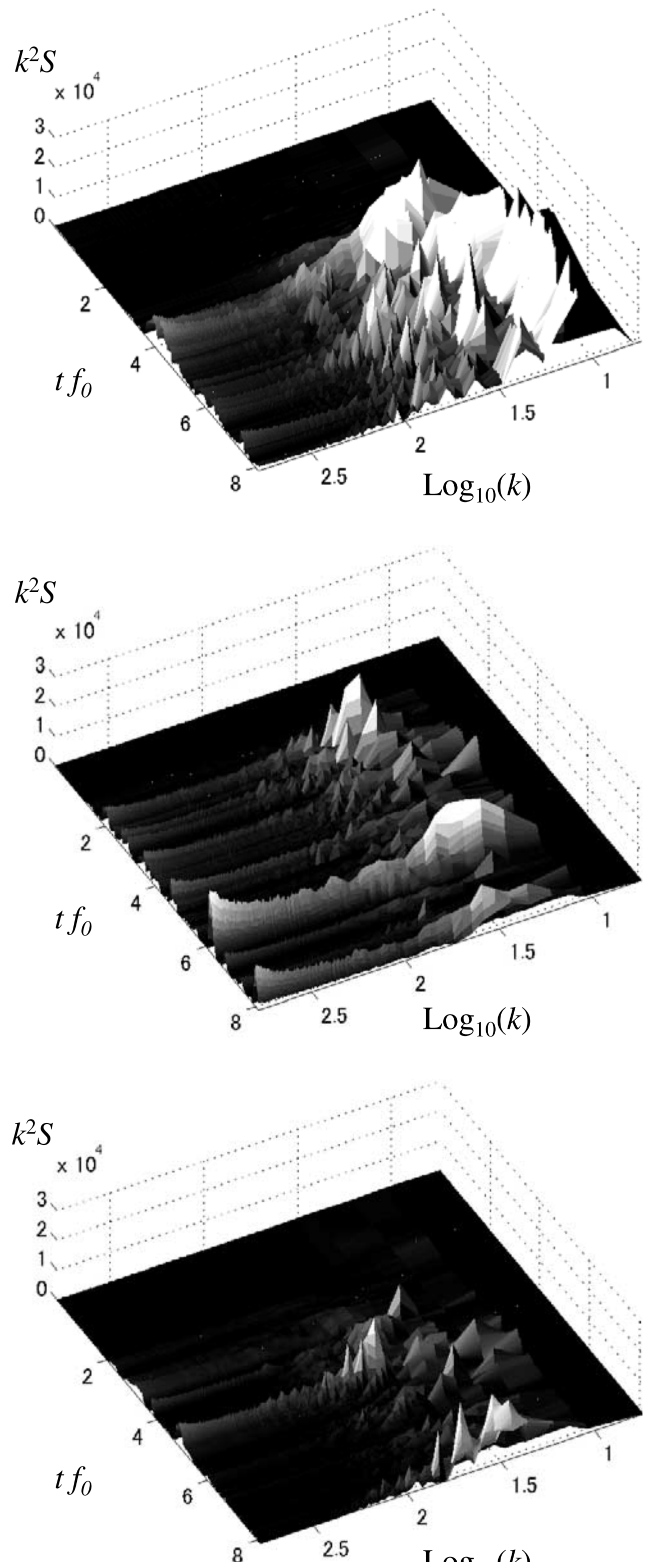

Figure 20. Time variations of the spanwise wave number spectra of temperature k^2S in small-scale experiments at (top) d = 11.3 cm (breaking region), (middle) 9.1 cm (plunging point), and (bottom) 6.2 cm (bore region) in run 4 (plunging breaker).

τ_d characterizes a mean transition time during which the initial temperature on a still water surface falls to an asymptotic value; this dimensional timescale substantially differs from the local timescales ($\tau_{renewal}/f_0$ and $\tau_{recovery}/f_0$) introduced in section 3.2 and Figure 17. For an exponential temperature decay, the constant a in (5) equals unity.

[54] For thermal diffusion resulting from skin-layer entrainment owing to subsurface turbulence, we assume that the turbulent kinetic energy $k \approx v_d^2$ and that the eddy viscosity $\nu_T \approx k^{1/2} l$, where l is the length scale of turbulence on the surface. Then the turbulent diffusivity may be written in terms of a turbulent Prandtl number ($Pr = \nu_T/D_T$) as

$$D_T \approx \frac{k^{1/2} l}{P_r} \approx \frac{1}{\tau_d}\left(\frac{al}{Pr}\right)^2. \tag{6}$$

A value for the timescale τ_d can be determined by fitting an exponential form to the decay of the mean surface temperature (see Figure 17). Because surface entrainment by counterrotating vortices is the major process that changes the surface temperature and that enhances three-dimensional thermal diffusion on the surface, we chose the characteristic length scale for surface turbulence l to be the mean interval between spanwise surface temperature patterns.

[55] Figure 19 shows cross-shore distributions of the turbulent thermal diffusivity D_T, estimated by (6), in plunging breakers (run 2) and in spilling breakers (run 6). In both types of breakers D_T was relatively low during early stages of the breaking process. In the transition region of plunging waves (x/d_b < 8), the diffusivity rapidly increased and became nearly constant in the bore region. In contrast, in spilling breakers, because of the gradual development of surface turbulence with propagation of breaking waves, the diffusivity increased monotonically from the breaking point. Although D_T for spilling breakers was always lower than for plunging waves, the values became comparable once a plunging wave entered the bore region (x/d_b > 8). This suggests (1) that the strong counterrotating vortices produced in plunging waves considerably enhance turbulent diffusion on the surface and (2) that turbulent bores in both plunging and spilling waves have the same effects on diffusion in the bore region.

[56] *Melville* [1994] found that the dissipation rate for a single wave-breaking event increases with wave slope (representing breaker type), but for multiple events the dissipation rate is approximately constant. Because dissipation rate occurs via a turbulent diffusion process, Melville's observations may explain the major features that we found for the thermal diffusivity: a single breaking event may dominate the behavior of the diffusivity during the early stages, but multiple events in the bore region may cause the diffusivities for both spilling and plunging breakers to be nearly constant and of similar magnitudes.

3.4. Scaling Laws for the Counterrotating Vortices

[57] Horizontal rollers are produced by consecutive splashing of water jets that project from surface gravitational waves; therefore, the sizes, intensities, and locations of primary roller vortices may be influenced by gravity. If so, they should be characterized by the Froude number (Fr = $U/\sqrt{gL}$); here U is a representative velocity scale and L is a representative length scale. Freely developing vortices are

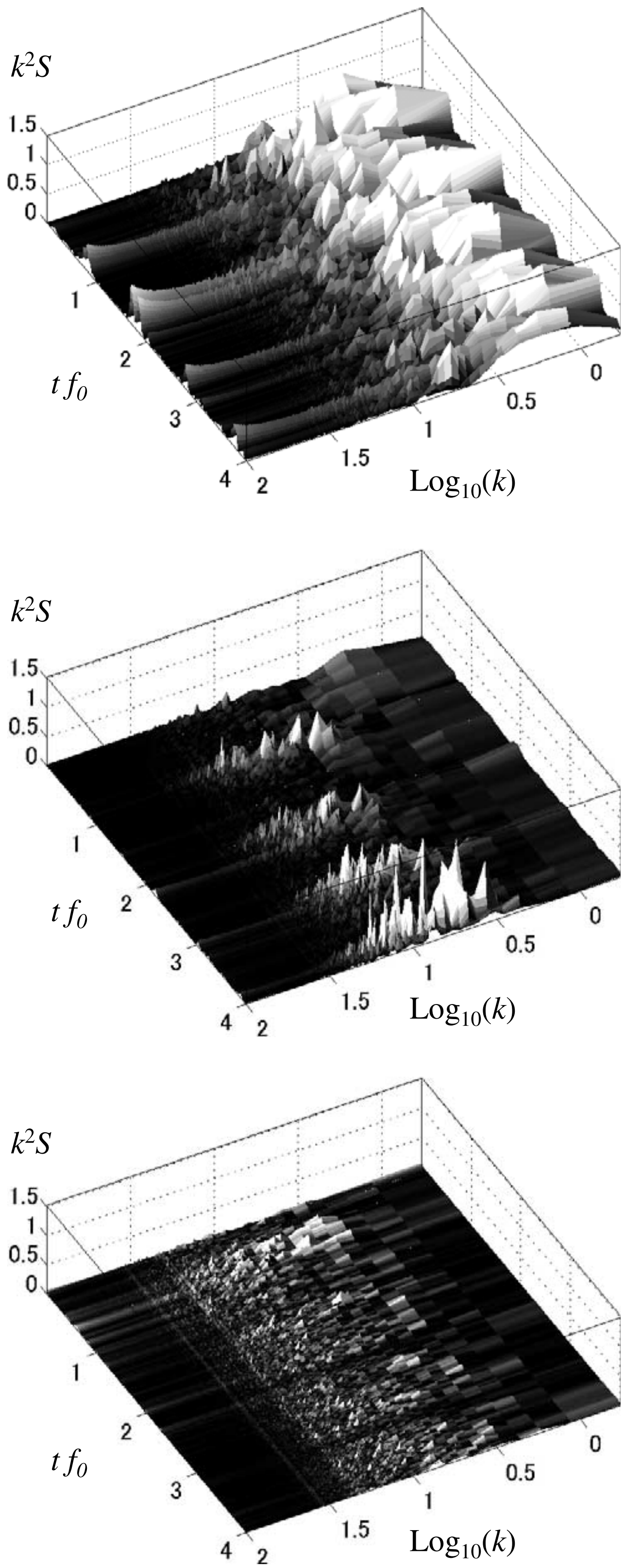

Figure 21. Time variations of the spanwise wave number spectra of temperature k^2S in large-scale experiments at (top) d = 92 cm (breaking point), (middle) 89 cm (plunging point), and (bottom) 60 cm (bore region) in run 9 (plunging breaker).

generally characterized by the Reynolds number (Re = UL/ν where ν is the kinematic viscosity); however, scaling parameters have yet to be determined for characterizing counterrotating vortices that originate between primary roller vortices in a gravity-dominated wavefield. In this section we use the spanwise wave number spectrum $S(k)$ of surface temperatures as the basis for discussing similarities among three-dimensional vortices in a surf zone and for identifying parameters that affect the evolution of vortices during wave breaking.

[58] As discussed in sections 3.1 and 3.2, subsurface vortex pairs were located by their infrared signatures. Because multiple pairs of counterrotating vortices occur below spanwise intervals of renewed surfaces, we can use those intervals to define a representative spanwise length (or size) for each vortex pair (see Figure 9). Figure 20 shows the temporal variation of k^2S for a plunging breaker (run 4) in the small-scale setup at the breaking point (depth d = 11.3 cm), at the plunging point (d = 9.1 cm), and in the bore region (d = 6.2 cm). The dominant spectra appear periodically in the range of $1.2 \le \log_{10}(k) \le 1.5$; this indicates that the typical spanwise length scales for subsurface counterrotating vortices are 3.16–6.3 cm (see also Figure 6). In the bore region, the spanwise lengths of vortices become shorter, in the range of 1.6–3.0 cm, because of turbulent bores (see also Figure 10).

[59] In the large-scale experiments, the corresponding spanwise length scales occur in the range of 10–31.6 cm for typical counterrotating vortices behind the plunging point (see Figure 21, and also Figure 7). As discussed in sections 3.1 and 3.2, the lengths of infrared signatures and the recovery times for large-scale experiments agreed with field observations by *Jessup* [1995] and *Jessup et al.* [1997]; however, we found considerable deviations for small-scale breaking waves.

[60] Figure 22 shows the ratio of the spanwise length and velocity scales in our small-scale and large-scale experiments at constant Fr and constant Re. As representative velocities, we used the wave celerity (c_p) of finite amplitude long waves with wave height H at water depth d,

$$c_p \equiv \sqrt{g(d+H)} = 1.256 \text{ m/s}, \tag{7}$$

for plunging breakers in the small-scale experiment, c_s = 0.90 m/s for spilling breakers in the small-scale experiment, and c_l = 2.87 m/s for breakers in the large-scale experiment. As representative length scales, we used the wavelength at each spectral peak: L_p = 5.0 cm, L_s = 3.0 cm and L_l = 25.0 cm. The relative vortex length scales for both plunging and spilling breakers were found to be on the line (in Figure 22) having Fr = constant; this suggests that the sizes of counterrotating vortices and the initial three-dimensional velocities at the surface are dominated by a gravitational wavefield and, hence, the phenomena may be characterized by the Froude number.

[61] As explained in section 3.2, the surface recovery process changes as breaking waves propagate (see Figure 18). We define a dimensionless frequency for the surface temperature by $f_T = 1/(\tau_{renewal} + \tau_{recovery})$; for turbulent bursting in an open-channel flow, this frequency corresponds to a so-called surface-renewal frequency that has been found

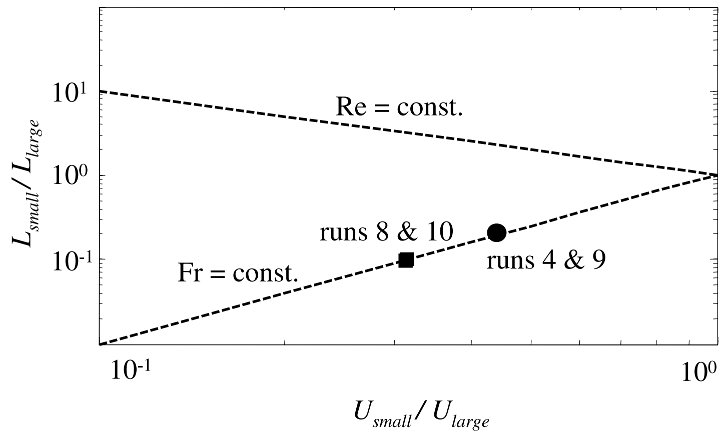

Figure 22. Relative length and velocity scales for counterrotating vortices in plunging (runs 4 and 9) and spilling (runs 8 and 10) breakers.

to correlate exponentially with Reynolds number [*Komori et al.*, 1989]. We have already discussed use of the Froude number to characterize surface renewal by large-scale vortices that are formed by dynamic splashing jets during the early stages of a plunging breaker. Further into the wave-breaking process, after the vortices have become less turbulent, small-scale turbulence is responsible for renewing the surface. Because the frequency f_T is approximately proportional to 3/2 power of Reynolds number (except during an initial stage of plunging wave breaking; see Figure 23), we should be able to determine f_T from the Reynolds number, not only when subsurface vortices have fully developed, but also when small-scale turbulence dominates the flow field. In passing we note that the slope of only two plots for the initial stage of plunging waves is roughly estimated to be about 2.

[62] The expression for turbulent diffusion in (6) may be rewritten in terms of a turbulent Reynolds number (Re_T),

$$D_T \approx \frac{k^{1/2} l}{P_r} \approx \frac{Re_T}{P_r} \nu_T. \tag{8}$$

Although the initial production of three-dimensional vortices is subject to a Froude scaling law, the mean surface thermal diffusivity (and hence, the relevant turbulent Reynolds number) increased as breaking waves propagate (see Figure 19). Because considerable turbulence develops at the surface of a bore region even for spilling breakers, the turbulent diffusivities in both kinds of breakers become comparable (Figure 19). This suggests that surface renewal owing to turbulent diffusion, characterized by a Reynolds number, becomes relatively significant for both kinds of breakers as breaking waves propagate. The regional difference of the mechanism for surface renewal changes the temperature modulation (section 3.2) and the increase rate of turbulent thermal diffusivity (section 3.3) during the wave-breaking process. Aeration may contribute considerably to turbulent diffusion in breaking waves; this issue remains to be investigated.

4. Conclusions

[63] We have used infrared measurements of surface temperatures as the basis for discussing the formation and evolution of subsurface vortices in breaking waves. After breaking waves pass the plunging point, bulk water of low temperature locally emerges onto the heated surface to form patch-like temperature regions at a certain spanwise interval; these cold patches stretch longitudinally to form a spanwise array. This organized pattern of surface temperature is induced by the same mechanism that forms scars near vortices beneath the surface; that is, above a horizontally located vortex, the surface layer is entrained into interior water and interior water near the vortex disrupts the surface layer by divergent surface flow, which renews the surface.

[64] In our large-scale experiments, the observed cold-water patches (wake length) assume sizes that are consistent with the lengths observed in situ by *Jessup* [1995]. In our small-scale experiments, however, the wake lengths deviate from the approximate relation between wake length and wave speed that was estimated by *Jessup* [1995].

[65] The experimental patterns we observed for surface temperatures have been confirmed by comparing them with computed results in which the distribution of longitudinal

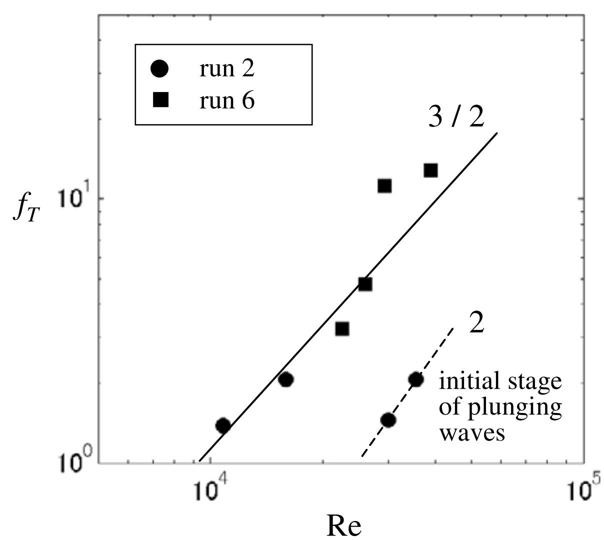

Figure 23. Correlation of surface-renewal frequency with Reynolds number for plunging (run 2) and spilling (run 6) breakers in small-scale experiments.

counterrotating vortices, located near the surface, correlate with a certain surface vorticity. The computed streamwise vorticity spectrum at the plunging point was found to be consistent with a temperature spectrum of cold patches on the surface; this demonstrates that streamwise counterrotating vortices, formed at the plunging point, cause the observed changes in surface temperature, and therefore such vortices are the underlying mechanism for surface renewal. The fractional area coverage of the renewed surface correlates with the root-mean square of the counterrotating vorticity on the surface in the both of plunging and bore regions, also indicating that the surface vorticity has a major role for renewing the surface in the surf zone.

[66] For both spilling and plunging breakers, we found that the time scale for surface recovery, estimated using the same definition as *Jessup et al.* [1997], lengthens as breaking waves propagate; however, cross-shore variations in renewal time depend on whether the breaker is plunging or spilling. During wave breaking, both recovery and renewal timescales are needed to characterize the surface disruption-restoration (or renewal-recovery) process.

[67] As breaking waves propagate, we found that the highest spanwise wave number spectra for surface temperatures occur at high wave numbers; this indicates that spanwise intervals become shorter as breaking waves propagate. These intervals correspond to a characteristic length scale for counterrotating subsurface vortices.

[68] The mean surface temperature tends to decrease exponentially with time, and the surface thermal diffusivity increases monotonically with wave propagation. During initial stages of wave breaking, turbulent thermal diffusivity in a plunging breaker is much higher than in a spilling breaker. Diffusivities for both spilling and plunging breakers become comparable on turbulent bores in bore regions.

[69] By comparing spanwise length scales for temperature variations at wave surfaces in small- and large-scale experiments, a scaling law was discussed for determining subsurface counterrotating vortices. The Froude number can be used to characterize the initial formation of longitudinal counterrotating vortices in a gravity-dominated splash-up process. For small-scale turbulent flows developed by wave breaking (in the bore region), the surface renewal frequency was found to correlate exponentially with Reynolds number.

[70] There are two different mechanisms for surface renewal that accompanies propagation of breaking waves. In the initial stage of wave breaking, gravity-induced vortices entrain the surface into interior of water to partially renew the surface along the vortices stretched on the rear face of waves in the plunging region. In contrast, in the bore region, the bore front containing strong turbulence precedes the wave crest to rapidly disturb and renew the whole surface in front of the wave crest.

Appendix A

[71] In the large-scale experiments performed in the open-air wave flume (see section 2.3), direct reflection of infrared rays from solar light affected our measurements for surface temperature. This can be verified by comparing infrared images in Figure 7 with visible images in the same figure. For example, in phase a of the top panel (infrared image) in Figure 7, we see a band of high temperatures aligned at x = 100 cm; for the same phase a in the bottom panel (visible image) we see a corresponding band of reflected light, also at x = 100 cm. Therefore, surface temperatures measured in our large-scale experiments contained some error because of surface reflection. In this appendix, we attempt to quantify that error.

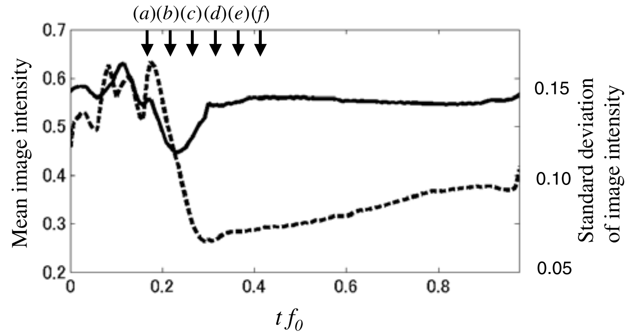

Figure A1. Mean visible-image intensity (solid line) and its standard deviation (broken line) in the large-scale experiment. The range of the gray scale image intensity is between 0 and 1. Phases a–f correspond to those in Figure 7.

[72] Figure A1 shows a time series for the spatially averaged, visible-image intensity, together with its standard deviation, during one wave period of a plunging breaking wave (run 9). The range of image intensity is between 0 and 1. The phases a–f in Figure A1 correspond to those in Figure 7. Because strongly reflected light is partially recorded when the view axis of the camera coincides with the path of reflection, high standard deviations (and therefore dispersion of the image intensity) appear when an image contains reflected light. Figure 23 shows that significant standard deviations over 25% of the mean image intensity appear for times tf_0 < 0.25; this corresponds to times when the overturning wave, with a curved surface, passes the measurement site (see also Figure 7). After the wave has passed, the standard deviation remains relatively small (5–10% of the mean intensity) until onset of the next wave breaking.

[73] Figure A2 shows spatially averaged, surface temperatures, with standard deviations plotted as error bars, for the same breaking wave as in Figure A1. Large errors (maximum range of 3.0°C), associated with reflection, are found in temperatures measured at times tf_0 < 0.25; this corresponds to the same duration of high standard deviation seen in the visible-image intensity in Figure A1. Note that the mean temperature is also affected by reflection. Figure A2 shows that the range of the error gradually increases from 1.0 to 1.5 °C after reflected wave faces have left the measurement site (tf_0 > 0.25); this can be attributed to surface disruption occurring as the surface is renewed (see Figure 15), as discussed in section 3.3.

[74] To reduce the contributions of reflection to our estimated mean temperatures, temperatures in reflected areas were eliminated if they were above a certain threshold (0.9°C higher than the mean bulk-water temperature 12.5°C). This process gave the solid line in Figure A2 for mean temperatures. The choice of the threshold (0.9°C) was based on the mean standard deviation for one wave period. The surface temperatures exceed the threshold are indicated

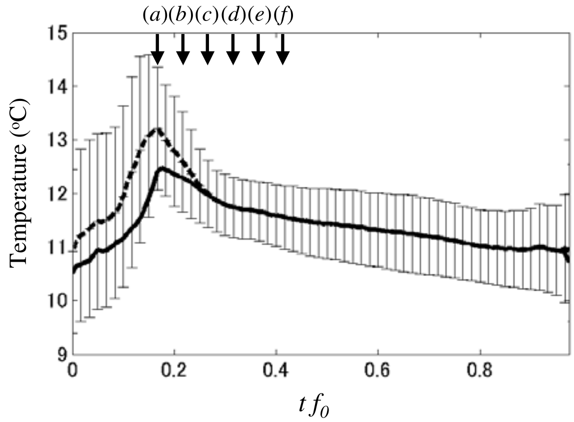

Figure A2. Mean surface temperature with error bars in the large-scale experiment; broken line: original measured temperature; solid line: mean temperature corrected for reflection-induced errors. Phases a–f correspond to those in Figure 7.

in Figure 7 and they should be excluded from the temperature statistics. It has been confirmed that the maximum difference of the mean temperature with and without this correction was less than the resolution limit (0.025°C) in the surface renewal term $tf_0 > 0.25$. Although large area on the overturning surface has been affected by sunlight reflection at the plunging phase a, there was less effect on the surface temperatures measured in the surface renewal phases c–f. However, in order to completely eliminate the solar reflection, measurements should be conducted under darkroom environment.

[75] **Acknowledgments.** The helpful comments of reviewers significantly helped to improve this manuscript. The authors are grateful to Nobukazu Tanaka of the Central Research Institute of Electric Power Industry (CRIEPI) in Japan for giving us permission to use the wave flume. We express our gratitude to David M. Ingram, who made helpful comments. This research was funded by the Ministry of Education, Science, Sports and Culture through Grant-in-Aid 17760409 (PI: N.M.), 18760368 (PI: Y.W.), bilateral research program (PI: Y.W.) and also the Sumitomo Foundation award 053493 (PI: N.M.).

References

Asher, W. E., A. T. Jessup, and M. A. Atmane (2004), Oceanic application of the active controlled flux technique for measuring air-sea transfer velocities of heat and gases, *J. Geophys. Res.*, *109*, C08S12, doi:10.1029/2003JC001862.

Branch, R., and A. T. Jessup (2007), Infrared signatures of microbreaking wave modulation, *IEEE Geosci. Remote Sens. Lett.*, *4*(3), 372–376.

Brocchini, M., and D. H. Peregrine (2001), The dynamics of strong turbulence at free surfaces. Part 1. Description, *J. Fluid Mech.*, *449*, 225–254.

Chang, K. A., and P. Liu (1999), Experimental investigation of turbulence generated by breaking waves in water of intermediate depth, *Phys. Fluids*, *11*, 3390–3400.

Cox, D. T., and N. Kobayashi (2000), Identification of intense, intermittent coherent motions under shoaling and breaking waves, *J. Geophys. Res.*, *105*(C6), 14,223–14,236.

Duncan, J. H. (2001), Spilling breaker, *Annu. Rev. Fluid Mech.*, *33*, 519–547.

Haußecker, H., B. Jähne, and S. Reinelt (1995), Heat as a proxy tracer for gas exchange measurements in the field: Principles and technical realization, in *Air-Water Gas Transfer*, pp. 405–413, Aeron-Verlag, Hanau, Germany.

Jähne, B., and H. Haußecker (1998), Air-water gas exchange, *Annu. Rev. Fluid Mech.*, *30*, 443–468.

Jeong, J.-T., and H. K. Moffat (1992), Free-surface cusps associated with flow at low Reynolds number, *J. Fluid Mech.*, *241*, 1–22.

Jessup, A. T. (1995), The infrared signature of breaking waves, in *Proceedings of the Fourth International Symposium on Air-Sea Interaction*, edited by M. A. Donelan, W. H. Hui, and W. J. Plant, pp. 665–670, Univ. of Toronto Press, Toronto, Ont., Canada.

Jessup, A. T., and V. Hesany (1996), Modulation of ocean skin temperature by swell waves, *J. Geophys. Res.*, *101*(C3), 6501–6511.

Jessup, A. T., C. Zappa, M. Lowen, and V. Hesany (1997), Infrared remote sensing of breaking waves, *Nature*, *385*, 52–55.

Komori, S., Y. Murakami, and H. Ueda (1989), The relationship between surface-renewal and bursting motions in an open-channel flow, *J. Fluid Mech.*, *203*, 103–123.

Longuet-Higgins, M. S. (1992), Capillary rollers and bores, *J. Fluid Mech.*, *240*, 659–679.

Melville, W. K. (1994), Energy dissipation by breaking waves, *J. Phys. Oceanogr.*, *24*, 2041–2049.

Melville, W. K., F. Veron, and C. J. White (2002), The velocity field under breaking waves: Coherent structures and turbulence, *J. Fluid Mech.*, *454*, 203–233.

Meola, C., and G. M. Carlomagno (2004), Recent advances in the use of infrared thermography, *Meas. Sci. Technol.*, *15*, R27–R58.

Nadaoka, K., M. Hino, and Y. Koyano (1989), Structure of the turbulent flow field under breaking waves in the surf zone, *J. Fluid Mech.*, *204*, 359–387.

Ohring, S., and H. Lugt (1991), Interaction of a viscous vortex pair with a free surface, *J. Fluid Mech.*, *227*, 47–70.

Okayasu, A., T. Shibayama, and N. Mimura (1986), Velocity field under plunging breaker, paper presented at 20th International Conference on Coastal Engineering, Am. Soc. of Civ. Eng., Taipei, Taiwan.

Sarpkaya, T. (1996), Vorticity, free surface and surfactants, *Annu. Rev. Fluid Mech.*, *28*, 83–128.

Siddiqui, M. H. K., M. R. Loewen, C. Richardson, W. E. Asher, and A. T. Jessup (2001), Simultaneous particle image velocimetry and infrared imagery of microscale breaking waves, *Phys. Fluids*, *13*, 1891–1903.

Straub, L. G., C. E. Bowers, and J. B. Herbich (1958), Laboratory tests of permeable wave absorbers, paper presented at 6th International Conference on Coastal Engineering, Am. Soc. of Civ. Eng., Reston, Va.

Ting, F. C. K., and J. T. Kirby (1995), Dynamics of surf-zone turbulence in a strong plunging breaker, *Coastal Eng.*, *24*, 177–204.

Ting, F. C. K., and J. T. Kirby (1996), Dynamics of surf-zone turbulence in a spilling breaker, *Coastal Eng.*, *27*, 131–160.

Watanabe, Y., H. Saeki, and R. J. Hosking (2005), Three-dimensional vortex structures breaking waves, *J. Fluid Mech.*, *545*, 291–328.

Wick, G. A., and A. T. Jessup (1998), Simulation of ocean skin temperature modulation by swell waves, *J. Geophys. Res.*, *103*(C2), 3149–3161.

Zappa, C. J., W. E. Asher, and A. T. Jessup (2004), Microbreaking and the enhancement of air-water transfer velocity, *J. Geophys. Res.*, *109*, C08S16, doi:10.1029/2003JC001897.

N. Mori, Disaster Prevention Research Institute, Kyoto University, Gokasho, Uji, Kyoto, Japan. (nobuhito.mori@hy5.ecs.kyoto-u.ac.jp)

Y. Watanabe, School of Engineering, Hokkaido University, North 13 West 8, Sapporo, Japan. (yasunori@eng.hokudai.ac.jp)